Simulation of viscous flows with undulatory boundaries. Part I: Basic solver

Di Yang, Lian Shen *

Department of Civil Engineering, Johns Hopkins University, Baltimore, MD 21218, USA

ARTICLE INFO

ABSTRACT

A numerical method for the simulation of viscous flows with undulatory walls and free surfaces is presented. The simulation domain is discretized by a boundary-fitted and time-dependent grid. The Navier–Stokes equations, subject to fully nonlinear kinematic and dynamic boundary conditions at the free surface and no-slip boundary condition at the wall, are simulated by a hybrid pseudo-spectral and finite difference method in space and a semi-implicit fractional-step method in time. The performance of the method is demonstrated by a series of test cases including flows over wavy boundaries, various surface waves, and interaction between vortices and free surfaces. Validation by convergence test and extensive comparisons with previous theoretical, experimental, and numerical studies indicate the accuracy and efficiency of the method. Finally, a simulation example of turbulence and free surface interaction is presented. Results show that the rich features of the free surface such as surface waves, splats, anti-splats, dimples, and scars are captured accurately. Characteristic vortical structures and variation of turbulence statistics in the near-surface region are also elucidated.

1. Introduction

Interaction of viscous flows, laminar or turbulent, with undulatory boundaries such as a waving wall and a free surface with wave motion is of interest to many fluid flow problems. Examples of important applications include wind over water waves [54,55], flow control by wavy plate [15,16,26,40], interactions of ocean turbulence with surface waves and internal waves [21,18], and damping of water waves by bottom mud flows [9,28]. To obtain a fundamental understanding of the mechanisms of these phenomena, it is desirable to have an accurate and efficient direct simulation tool for viscous flows with undulatory boundaries.

For flows with complex boundaries, methods based on fixed Eulerian grid have been found effective. For example, the immersed boundary method (see e.g. [30]) has been applied to flows near wavy boundaries [46,47,52]; the level-set method (see e.g. [38]), the group of methods based on a front-tracking approach (see e.g. [44,48]), and the volume-of-fluid method (see e.g. [36]) have been used to simulate flows with free surfaces. If the detailed flow structures near the boundaries need to be resolved, methods based on boundary-fitted grid with grid clustering near the boundary layers are desirable. In many previous studies (see e.g. [5,6,7,13,21,24,58,59,60]), orthogonal or non-orthogonal grids are used in the physical space to follow the curvature of the moving wavy boundaries.

In the present study, we aim at developing a numerical method that is capable of accurately resolving the fine details at the undulatory boundaries. Viscous flows interacting with waves with moderate steepness is the main focus of the applications. Our numerical scheme is based on the specific physics of the problems. First, because the waves have finite amplitude and are non-breaking, we apply an effective boundary-fitted grid that follows the wavy boundary motion based on algebraic

mapping. Second, in many applications, strong shear is present at the boundaries including the free surfaces (due to e.g. wind blowing). Clustered grid near the boundaries is needed to resolve the boundary layers adequately, which makes the explicit time-integration schemes for viscous terms used in many previous free-surface simulations (e.g. [13,63]) unsuitable here because of the constraint on the timestep by the small grid size. In the present study, we adopt the fractional-step method [23] in which a semi-implicit scheme is used for the viscous terms. Because of the nonlinear terms caused by the grid mapping, substantial complexities are introduced to the problem and require special treatment. Third, the deformable free surface produces complex physics such as the effects of nonlinear wave interactions and surface vorticity [35,45,57]. Therefore, precise computation of the surface evolution is required, in addition to the accurate simulation of the Navier–Stokes equations [53]. In the present study, the spatial discretization in the horizontal directions is realized by a spectral method, so that the surface elevation is accurately resolved up to high order [63]. We use an explicit scheme to advance the surface deformation in time subject to the fully nonlinear kinematic free-surface boundary condition. The location of the free surface at the new timestep then establishes a basis for the grid mapping for the simulation of the Navier–Stokes equations. Special care is taken to ensure the consistence in the accuracy of the free surface evolution, the simulation of the Navier–Stokes equations, and the boundary condition treatment.

Besides the development of numerical method, another goal of this study is to perform systematic tests for various flows with undulatory surfaces to document the various aspects of the simulation performance. In this paper, we present comprehensive test results for flows over wavy boundaries, various surface waves, vortex and free surface interaction, and interaction between turbulence and free surface. Quantitative comparisons with the data in the literature are performed and good agreement is obtained. These cases may be used for the numerical test of other methods for similar applications in the future.

This paper is organized as follows: Section 2 discusses the numerical scheme. Section 3 documents the test cases and the results for validation. Finally, conclusions are given in Section 4.

2. Numerical method

2.1. Problem definition and governing equations

The present study aims at simulating fluid problems involving undulatory boundaries, which can be located at the top of the computational domain (e.g. simulation of water motion below ocean surface waves), at the bottom of the domain (e.g. simulation of wind over water waves), or at both the top and the bottom (e.g. simulation of water motion between surface waves and the lutocline above bottom mud flow). To take into account the general situation, we consider the physical domain shown in Fig. 1(a), which is bounded by a top wavy free surface and a bottom undulatory boundary. We set the x- and y-axes to be horizontal, the z-axis to be vertical, and the origin to be located at the mean level of the top surface. The deformation of the top surface is denoted by $\eta(x, y, t)$; $H(x, y, t)$ is the height of the domain from $z = 0$ to the bottom boundary, which is further decomposed into a mean height $\overline{H}$ and a variation component $H'(x, y, t)$.

We consider the incompressible fluid with density ρ and kinematic viscosity ν governed by the Navier–Stokes equations and continuity equation
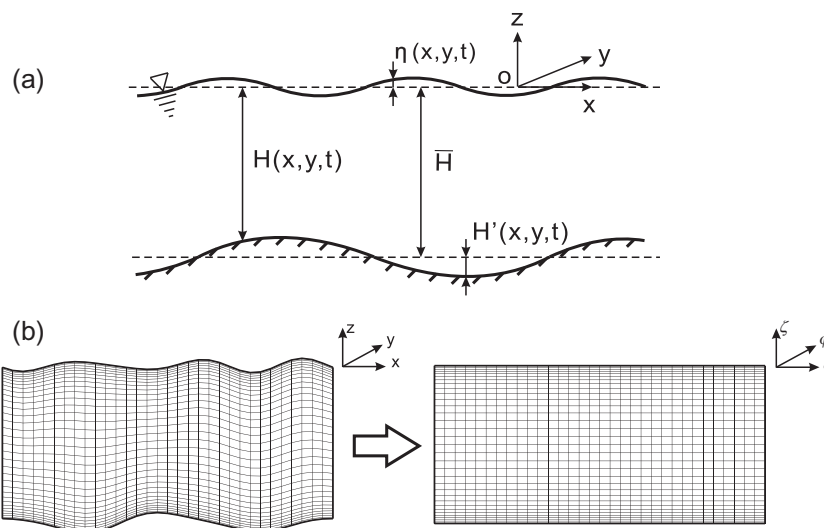
Fig. 1. Illustration of coordinate transformation. The irregular physical domain in the (x, y, z, t) space is transformed to a right rectangular prism in the computational domain $(\xi, \varphi, \zeta, \tau)$. Only a vertical cross-section in the three dimensional space is plotted here.

$$\frac{\partial u_i}{\partial t} + \frac{\partial (u_i u_j)}{\partial x_j} = -\frac{1}{\rho}\frac{\partial p}{\partial x_i} + \nu \frac{\partial^2 u_i}{\partial x_j \partial x_j}, \tag{1}$$

$$\frac{\partial u_i}{\partial x_i} = 0. \tag{2}$$

Here, u_i $(i = 1, 2, 3) = (u, v, w)$ are the velocity components in the x-, y-, and z-directions, respectively; p is the dynamic pressure, which is related to the total pressure P through $p = P + \rho g z$ with g the gravitational acceleration.

In order to adequately resolve the flow details near the undulatory boundaries, we employ a boundary-fitted grid. As shown in Fig. 1(b), the irregular physical domain in the (x, y, z, t) space is transformed to a right rectangular prism in the computational domain $(\xi, \varphi, \zeta, \tau)$ with the following algebraic mapping:

$$\xi = x, \quad \varphi = y, \quad \zeta = \frac{z + H(x, y, t)}{\eta(x, y, t) + H(x, y, t)} = \frac{z + \overline{H} + H'(x, y, t)}{\eta'(x, y, t) + \overline{H}}, \quad \tau = t, \tag{3}$$

where $\eta' = \eta + H'$. The Jacobian matrix of the mapping is

$$J = \begin{bmatrix} \xi_x & \xi_y & \xi_z & \xi_t \\ \varphi_x & \varphi_y & \varphi_z & \varphi_t \\ \zeta_x & \zeta_y & \zeta_z & \zeta_t \\ \tau_x & \tau_y & \tau_z & \tau_t \end{bmatrix} = \begin{bmatrix} 1 & 0 & 0 & 0 \\ 0 & 1 & 0 & 0 \\ \frac{H'_x - \zeta\eta'_x}{\eta' + \overline{H}} & \frac{H'_y - \zeta\eta'_y}{\eta' + \overline{H}} & \frac{1}{\eta' + \overline{H}} & \frac{H'_t - \zeta\eta'_t}{\eta' + \overline{H}} \\ 0 & 0 & 0 & 1 \end{bmatrix}, \tag{4}$$

where the subscripts denote the partial derivatives. This coordinate transformation has been used in atmospheric and oceanic applications (see e.g. [11,20]). By applying the chain rule, we obtain the following transformation of derivatives

$$\left. \begin{aligned} \frac{\partial}{\partial x} &= \frac{\partial}{\partial \xi} + \zeta_x \frac{\partial}{\partial \zeta}, \\ \frac{\partial}{\partial y} &= \frac{\partial}{\partial \varphi} + \zeta_y \frac{\partial}{\partial \zeta}, \\ \frac{\partial}{\partial z} &= \zeta_z \frac{\partial}{\partial \zeta}, \\ \frac{\partial}{\partial t} &= \frac{\partial}{\partial \tau} + \zeta_t \frac{\partial}{\partial \zeta}. \end{aligned} \right\} \tag{5}$$

We substitute the operators (5) into Eqs. (1) and (2), and obtain the governing equations in the computational space

$$\frac{\partial u}{\partial \tau} + \zeta_t \frac{\partial u}{\partial \zeta} + \frac{\partial (uu)}{\partial \xi} + \zeta_x \frac{\partial (uu)}{\partial \zeta} + \frac{\partial (uv)}{\partial \varphi} + \zeta_y \frac{\partial (uv)}{\partial \zeta} + \zeta_z \frac{\partial (uw)}{\partial \zeta} = -\frac{1}{\rho}\left(\frac{\partial p}{\partial \xi} + \zeta_x \frac{\partial p}{\partial \zeta}\right) + \nu \nabla^2 u, \tag{6}$$

$$\frac{\partial v}{\partial \tau} + \zeta_t \frac{\partial v}{\partial \zeta} + \frac{\partial (uv)}{\partial \xi} + \zeta_x \frac{\partial (uv)}{\partial \zeta} + \frac{\partial (vv)}{\partial \varphi} + \zeta_y \frac{\partial (vv)}{\partial \zeta} + \zeta_z \frac{\partial (vw)}{\partial \zeta} = -\frac{1}{\rho}\left(\frac{\partial p}{\partial \varphi} + \zeta_y \frac{\partial p}{\partial \zeta}\right) + \nu \nabla^2 v, \tag{7}$$

$$\frac{\partial w}{\partial \tau} + \zeta_t \frac{\partial w}{\partial \zeta} + \frac{\partial (uw)}{\partial \xi} + \zeta_x \frac{\partial (uw)}{\partial \zeta} + \frac{\partial (vw)}{\partial \varphi} + \zeta_y \frac{\partial (vw)}{\partial \zeta} + \zeta_z \frac{\partial (ww)}{\partial \zeta} = -\frac{1}{\rho}\left(\zeta_z \frac{\partial p}{\partial \zeta}\right) + \nu \nabla^2 w, \tag{8}$$

$$\frac{\partial u}{\partial \xi} + \zeta_x \frac{\partial u}{\partial \zeta} + \frac{\partial v}{\partial \varphi} + \zeta_y \frac{\partial v}{\partial \zeta} + \zeta_z \frac{\partial w}{\partial \zeta} = 0, \tag{9}$$

where the Laplacian operator is decomposed into $\nabla^2 = \nabla^2_{\xi\varphi} + \nabla^2_{\zeta}$ as:

$$\nabla^2_{\xi\varphi} = \frac{\partial^2}{\partial \xi^2} + \frac{\partial^2}{\partial \varphi^2} + 2\zeta_x \frac{\partial^2}{\partial \xi \partial \zeta} + 2\zeta_y \frac{\partial^2}{\partial \varphi \partial \zeta}, \tag{10}$$

$$\nabla^2_{\zeta} = \left(\frac{H'_{xx} - \zeta\eta'_{xx} + H'_{yy} - \zeta\eta'_{yy}}{\eta' + \overline{H}} - 2\zeta_x\zeta_z\eta'_x - 2\zeta_y\zeta_z\eta'_y\right)\frac{\partial}{\partial \zeta} + (\zeta_x^2 + \zeta_y^2 + \zeta_z^2)\frac{\partial^2}{\partial \zeta^2}. \tag{11}$$

We note that the velocities (u, v, w) in the above equations are still defined based on the velocity vectors in (x, y, z, t) space, and the algebraic mapping equation (3) is not conformal. This approach is justified by the physical problems we focus on, in which the wave surfaces do not have too steep or overturning geometries. In some of the previous studies, conformal mapping was used to simulate flows with complex boundary geometries. As pointed out by Hodges and Street [21], the conformal mapping is accurate but complex and costly, and is unnecessary if the surface is not steep. Refs. [31,34] showed that the error due to the grid non-orthogonality is small for grid distortion angle less than 40°. For the physical problems considered in this study, the surface inclination angle is typically less than 20°, and the grid distortion caused by the algebraic mapping equation (3) does not cause problem in all the tests we have performed.

2.2. Boundary conditions

In this study, periodic boundary conditions are used in the horizontal directions. In the following subsections, we discuss the boundary conditions at the top and the bottom undulatory boundaries.

2.2.1. Top boundary conditions

For the problems in question, the top boundary is usually a free surface with elevation η (for the special situation of a flat surface, we simply set $\eta = 0$). The kinematic boundary condition (KBC) states that the free surface is material:

$$\eta_t = w - u\eta_x - v\eta_y \quad \text{at } z = \eta. \tag{12}$$

In our simulation, (12) is integrated in time to upgrade the free-surface deformation and the associated grid mapping.

The dynamic boundary condition (DBC) specifies the stress balance at the free surface. The stress components in the surface-normal and surface-tangential directions are expressed as

$$\sigma_{\mathbf{n}} = \mathbf{n} \cdot [\boldsymbol{\sigma}] \cdot \mathbf{n}^{\mathrm{T}}, \quad \sigma_{\mathbf{t1}} = \mathbf{t}_1 \cdot [\boldsymbol{\sigma}] \cdot \mathbf{n}^{\mathrm{T}}, \quad \sigma_{\mathbf{t2}} = \mathbf{t}_2 \cdot [\boldsymbol{\sigma}] \cdot \mathbf{n}^{\mathrm{T}}. \tag{13a, b, c}$$

Here $[\boldsymbol{\sigma}]$ is the stress tensor expressed as $[\sigma]_{ij} = -P\delta_{ij} + \rho v(u_{i,j} + u_{j,i})$, with δ_{ij} the Kronecker delta. The superscript 'T' denotes the transpose of the vector. And $\mathbf{n}$ is the unit vector in the outer-pointing (with respect to the simulation domain) normal direction of the free surface; $\mathbf{t}_1$ and $\mathbf{t}_2$ are the unit vectors tangential to the free surface in the (x, z)-and (y, z)-planes, respectively. These surface direction vectors are expressed as

$$\mathbf{n} = \frac{(-\eta_x, -\eta_y, 1)}{\sqrt{\eta_x^2 + \eta_y^2 + 1}}, \quad \mathbf{t}_1 = \frac{(1, 0, \eta_x)}{\sqrt{\eta_x^2 + 1}}, \quad \mathbf{t}_2 = \frac{(0, 1, \eta_y)}{\sqrt{\eta_y^2 + 1}}. \tag{14}$$

The stress balance at the free surface requires that

$$\sigma_{\mathbf{n}} = \sigma_{\mathbf{n}}|_{\text{external}} + \gamma \frac{(1 + \eta_x^2)\eta_{yy} + (1 + \eta_y^2)\eta_{xx} - 2\eta_x\eta_y\eta_{xy}}{(1 + \eta_x^2 + \eta_y^2)^{3/2}}, \tag{15}$$

$$\sigma_{\mathbf{t}i} = \sigma_{\mathbf{t}i}|_{\text{external}}, \quad i = 1, 2, \tag{16}$$

where the subscript 'external' denotes the other side of the free surface (e.g. airside for the water wave simulation), and γ is the surface tension.

By substituting Eqs. (13a,b,c) and (14) into conditions (15) and (16) and by applying the transformation (5) and continuity equation (9), we obtain the Dirichlet boundary condition for the pressure

$$p = \rho g\eta + \frac{2\rho v}{(1 + \eta_x^2 + \eta_y^2)}\left\{-(1 + \eta_y^2)\frac{\partial u}{\partial \xi} - (1 + \eta_x^2)\frac{\partial v}{\partial \varphi} + \eta_x\eta_y\left(\frac{\partial u}{\partial \varphi} + \frac{\partial v}{\partial \xi}\right) - \eta_x\frac{\partial w}{\partial \xi} - \eta_y\frac{\partial w}{\partial \varphi}\right\} - \sigma_{\mathbf{n}}|_{\text{external}}$$

$$- \gamma \frac{(1 + \eta_x^2)\eta_{yy} + (1 + \eta_y^2)\eta_{xx} - 2\eta_x\eta_y\eta_{xy}}{(1 + \eta_x^2 + \eta_y^2)^{3/2}} \quad \text{at } z = \eta, \tag{17}$$

and the Neumann boundary conditions for the velocity components

$$\frac{\partial u}{\partial \zeta} = C_0\left\{C_1^1\left(\frac{\partial u}{\partial \varphi} + \frac{\partial v}{\partial \xi}\right) + C_2^1\frac{\partial u}{\partial \xi} + C_3^1\frac{\partial v}{\partial \varphi} + C_4^1\frac{\partial w}{\partial \xi} + C_5^1\frac{\partial w}{\partial \varphi} + C_6^1\frac{\sigma_{\mathbf{t1}}|_{\text{external}}}{\rho v} + C_7^1\frac{\sigma_{\mathbf{t2}}|_{\text{external}}}{\rho v}\right\} \quad \text{at } z = \eta, \tag{18}$$

$$\frac{\partial v}{\partial \zeta} = C_0\left\{C_1^2\left(\frac{\partial u}{\partial \varphi} + \frac{\partial v}{\partial \xi}\right) + C_2^2\frac{\partial u}{\partial \xi} + C_3^2\frac{\partial v}{\partial \varphi} + C_4^2\frac{\partial w}{\partial \xi} + C_5^2\frac{\partial w}{\partial \varphi} + C_6^2\frac{\sigma_{\mathbf{t1}}|_{\text{external}}}{\rho v} + C_7^2\frac{\sigma_{\mathbf{t2}}|_{\text{external}}}{\rho v}\right\} \quad \text{at } z = \eta, \tag{19}$$

$$\frac{\partial w}{\partial \zeta} = -\left\{(\eta + H)\frac{\partial u}{\partial \xi} - \eta_x\frac{\partial u}{\partial \zeta} + (\eta + H)\frac{\partial v}{\partial \varphi} - \eta_y\frac{\partial v}{\partial \zeta}\right\} \quad \text{at } z = \eta. \tag{20}$$

Here,

$$C_0 = \frac{\eta + H}{(1 + \eta_x^2 + \eta_y^2)^2}, \tag{21}$$

$$\begin{cases} C_1^1 = \eta_y(1 - \eta_x^2 + \eta_y^2), \quad C_2^1 = \eta_x(3 + \eta_x^2 + 3\eta_y^2), \\ C_3^1 = \eta_x(1 + \eta_x^2 - \eta_y^2), \quad C_4^1 = -(1 - \eta_x^2 + \eta_y^2), \quad C_5^1 = 2\eta_x\eta_y, \\ C_6^1 = (1 + \eta_y^2)\sqrt{(\eta_x^2 + \eta_y^2 + 1)(\eta_x^2 + 1)}, \\ C_7^1 = -\eta_x\eta_y\sqrt{(\eta_x^2 + \eta_y^2 + 1)(\eta_y^2 + 1)}, \end{cases} \tag{22}$$

$$\begin{cases} C_1^2 = \eta_x(1 + \eta_x^2 - \eta_y^2), \quad C_2^2 = \eta_y(1 - \eta_x^2 + \eta_y^2), \\ C_3^2 = \eta_y(3 + 3\eta_x^2 + \eta_y^2), \quad C_4^2 = 2\eta_x\eta_y, \quad C_5^2 = -(1 + \eta_x^2 - \eta_y^2), \\ C_6^2 = -\eta_x\eta_y\sqrt{(\eta_x^2 + \eta_y^2 + 1)(\eta_x^2 + 1)}, \\ C_7^2 = (1 + \eta_x^2)\sqrt{(\eta_x^2 + \eta_y^2 + 1)(\eta_y^2 + 1)}. \end{cases} \tag{23}$$

2.2.2. Bottom boundary condition

At the bottom boundary, we assume its geometry and velocity are prescribed:

$$\begin{cases} H' = -\eta_b, \\ (u, v, w) = (u_b, v_b, w_b) \quad \text{at } z = -H, \end{cases} \tag{24}$$

where the subscript 'b' denotes the variables at the bottom boundary. The above Dirichlet conditions are chosen because in our applications such as wind over waves, the air is much lighter than the water and sees the water surface as a moving solid boundary [3,10,55]. Even for the internal wave problem where the densities of the different layers of the fluids do not differ much, the coupling of Eq. (24) for the upper layer with the stress-driven conditions given in Eqs. (15) and (16) for the lower layer using an iterative coupling method still ensures the continuity of velocity and the balance of stress at the interface (for details of this coupling see the companion paper [56]).

We remark that the above Dirichlet bottom boundary condition is specified particularly for the physical problems considered in the present study. For more general problems, a set of KBC and DBC for the bottom boundary can be obtained in a way similar to the analysis in Section 2.2.1. In doing so, the surface elevation η in Eqs. (12), (13a)–(c), (14)–(23) should be replaced by $-H'$ accordingly. The implementation of numerical discretizations is similar to the top boundary case and is straightforward.

2.3. Numerical scheme

2.3.1. Spatial discretization

In this study, we use a Fourier-series-based pseudo-spectral method for the spatial discretization in the horizontal directions. The computational domain is discretized by equally spaced grid in the ξ- and φ-directions (labeled by the indices i and j, respectively), as shown in Fig. 2(a). We use the 2/3 rule to treat the aliasing error in the pseudo-spectral method. In the vertical direction, we use a second-order finite difference scheme on a staggered grid [39], as shown in Fig. 2(b). In the vertical direction, the regular grid points are labeled by k, while the staggered grid points are labeled by k^*. The variables u, v, and p are defined on the regular grid (i, j, k), while w is defined on the vertically-staggered grid (i, j, k^*).

2.3.2. Free surface evolution

In the simulation, the free surface elevation η is updated by advancing Eq. (12) with a second-order Runge–Kutta (RK2) scheme [62]:

- step 1:

$$\eta_t^{(n)} = w^{(n)} - u^{(n)}\eta_x^{(n)} - v^{(n)}\eta_y^{(n)}, \tag{25}$$

$$\eta^{(n+1)^*} = \eta^{(n)} + \Delta t\eta_t^{(n)}, \tag{26}$$

- step 2:

$$\eta_t^{(n+1)^*} = w^{(n+1)^*} - u^{(n+1)^*}\eta_x^{(n+1)^*} - v^{(n+1)^*}\eta_y^{(n+1)^*}, \tag{27}$$

$$\eta^{(n+1)} = \eta^{(n+1)^*} + \frac{\Delta t}{2}\left(\eta_t^{(n+1)^*} - \eta_t^{(n)}\right). \tag{28}$$

Hereinafter, the superscripts '(n)' and '$(n+1)$' denote the variables at the timesteps (n) and $(n+1)$, respectively; and the superscript '$(n+1)^*$' denotes the variables after the first step of the RK2 method.

At each timestep, firstly $\eta^{(n+1)^*}$ is calculated using Eqs. (25) and (26), and the corresponding grid mapping is calculated. Eqs. (6)–(9) are solved on this $\eta^{(n+1)^*}$-based grid to obtain $u_i^{(n+1)^*}$ [13,21,62] (details of the solver are given in Section 2.3.3). Then $\eta^{(n+1)^*}$ is updated to $\eta^{(n+1)}$ using Eqs. (27) and (28). The value of $u_i^{(n+1)}$ is solved on the $\eta^{(n+1)}$-based grid and the simulation advances to the next timestep.

2.3.3. Navier–Stokes solver

The Navier–Stokes equations (6)–(9) are integrated in time based on a fractional-step method [2,23,61]. Similar to Kim and Moin [23],
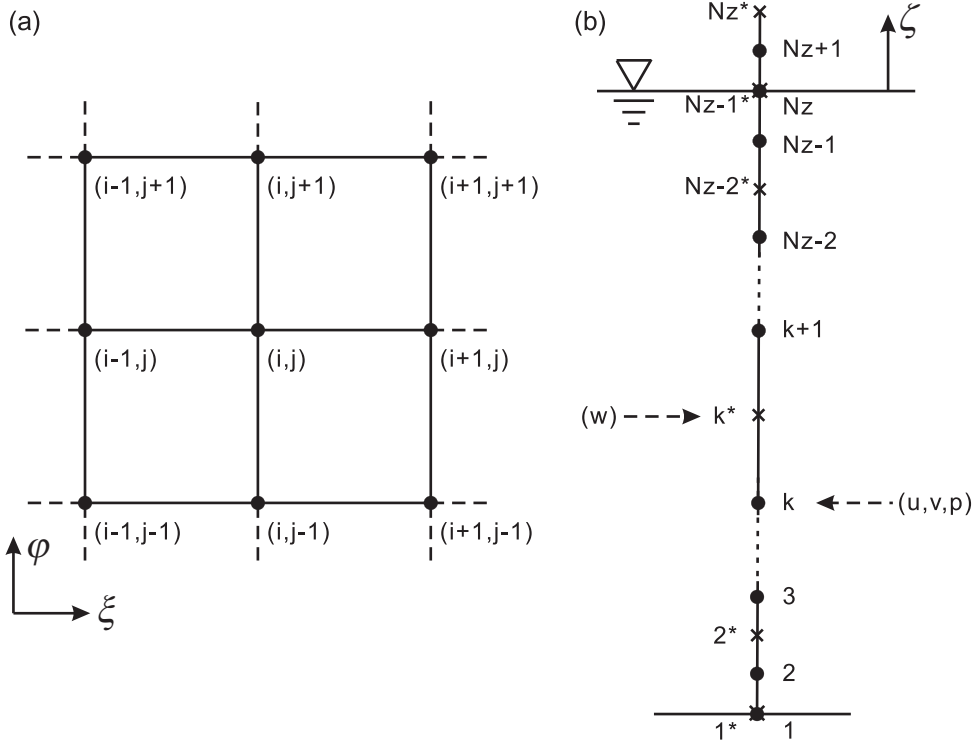
Fig. 2. Illustration of grid in the computational space. In the horizontal directions as plotted in (a), a uniform grid is used, with all the variables defined on the grid points. In the vertical direction as plotted in (b), a staggered grid is used, with variables u, v, and p defined on the grid points denoted by •, and variable w defined on the grid points denoted by ×.

$$\frac{\hat{u}_i - u_i^{(n)}}{\Delta t} + \zeta_t \frac{\partial}{\partial \zeta}\left(\frac{\hat{u}_i + u_i^{(n)}}{2}\right) = \frac{3R_i^{(n)} - R_i^{(n-1)}}{2} + \nu \nabla_\zeta^2\left(\frac{\hat{u}_i + u_i^{(n)}}{2}\right),$$ (29)

$$u_i^{(n+1)} = \hat{u}_i - \frac{\Delta t}{\rho}\frac{\partial \wp}{\partial x_i}^{(n+1)},$$ (30)

with

$$\frac{\partial u_i^{(n+1)}}{\partial x_i} = 0.$$ (31)

Here, the hat denotes the variables at the intermediate step of the fractional-step method. A Crank–Nicolson (CN) scheme is used for the ∇_ζ^2-component of the viscous terms (Eq. 11), and a second-order Adams–Bashforth (AB2) scheme is used for the convective terms and the $\nabla_{\xi\varphi}^2$-component of the viscous terms (Eq. 10). The term $R_i^{(n)}$ is expressed as

$$R_i^{(n)} = -\frac{\partial(u_iu)^{(n)}}{\partial \xi} - \zeta_x^{(n)}\frac{\partial(u_iu)^{(n)}}{\partial \zeta} - \frac{\partial(u_iv)^{(n)}}{\partial \varphi} - \zeta_y^{(n)}\frac{\partial(u_iv)^{(n)}}{\partial \zeta} - \zeta_z^{(n)}\frac{\partial(u_iw)^{(n)}}{\partial \zeta} + \nu \nabla_{\xi\varphi}^2 u_i^{(n)}.$$ (32)

Eq. (29) is rewritten as

$$\nabla_\zeta^2 \hat{u}_i - \frac{2\hat{u}_i}{\nu\Delta t} - \frac{\zeta_t}{\nu}\frac{\partial \hat{u}_i}{\partial \zeta} = -\frac{1}{\nu}\left(3R_i^{(n)} - R_i^{(n-1)}\right) - \nabla_\zeta^2 u_i^{(n)} - \frac{2u_i^{(n)}}{\nu\Delta t} - \frac{\zeta_t}{\nu}\frac{\partial u_i^{(n)}}{\partial \zeta}.$$ (33)

Note that different from [23], the viscous terms in the ζ-direction and the other two directions are treated by the CN and AB2 schemes, respectively [29,61]. With a second-order central difference scheme in the z-direction for Eq. (33), the velocity at the intermediate step, $\hat{u}_i$, is solved through a tridiagonal linear equation system. Meanwhile, the semi-implicit scheme is still used for the dominant viscous terms $\nabla_\zeta^2 u_i$ to allow the fine resolution of the boundary layer without the penalty of the small viscous timestep. This modification of the fractional-step method is found to be computationally efficient for the study of turbulence–wave interaction [55].

The scalar $\wp$ in Eq. (30), called pseudo-pressure, is related to the dynamic pressure by [23]

$$p^{(n+1/2)} = \wp^{(n+1)} - \frac{\rho\nu\Delta t}{2}\nabla^2\wp^{(n+1)}.$$ (34)

By applying the divergence operator to Eq. (30) and substituting Eq. (31) into it, we obtain a Poisson equation for the pseudo-pressure:

$$\nabla^2 \wp^{(n+1)} = -\frac{\rho}{\Delta t}\frac{\partial \hat{u}_i}{\partial x_i}. \tag{35}$$

This Poisson equation is solved to obtain $\wp^{(n+1)}$. It is noted that the Laplacian operator in Eq. (35) is nonlinear because of the algebraic mapping. With the pseudo-spectral method in the horizontal directions, Eq. (35) needs to be solved iteratively. After substituting Eq. (5) into Eq. (35), we rewrite the nonlinear Poisson equation as

$$\frac{\partial^2 \wp}{\partial \xi^2}^{[m+1]} + \frac{\partial^2 \wp}{\partial \varphi^2}^{[m+1]} + \frac{1}{H^2}\frac{\partial^2 \wp}{\partial \zeta^2}^{[m+1]} = -2\zeta_x^{(n+1)}\frac{\partial^2 \wp}{\partial \xi \partial \zeta}^{[m]} - 2\zeta_y^{(n+1)}\frac{\partial^2 \wp}{\partial \varphi \partial \zeta}^{[m]} - \nabla_\zeta^{2\,(n+1)}\wp^{[m]} + \frac{1}{H^2}\frac{\partial^2 \wp}{\partial \zeta^2}^{[m]}$$
$$+ \frac{\rho}{\Delta t}\left(\frac{\partial \hat{u}}{\partial \xi} + \zeta_x^{(n+1)}\frac{\partial \hat{u}}{\partial \zeta} + \frac{\partial \hat{v}}{\partial \varphi} + \zeta_y^{(n+1)}\frac{\partial \hat{v}}{\partial \zeta} + \zeta_z^{(n+1)}\frac{\partial \hat{w}}{\partial \zeta}\right). \tag{36}$$

Here the superscripts '[m]' and '[m + 1]' denote the previous and current iteration steps, respectively; and the superscript '(n + 1)' denotes timestep as in Eq. (28). With the spectral method in the horizontal directions, each Fourier mode in Eq. (36) is now decoupled from the others and can be solved in the z-direction through a tridiagonal linear equation system. A modified Newton's method [40,62] is employed, which uses the values from the previous two steps to accelerate the convergence of iteration. For the simulations studied in this paper, the relative residual error in $\wp$ is reduced to less than 10^{-10} within six iterations (typically it takes two to four iterations).

After Eq. (36) is solved, the solution $\wp^{(n+1)}$ is used to update the velocity from $\hat{u}_i$ to $u_i^{(n+1)}$. The velocity at timestep $(n + 1)$ is thus divergence free.

2.3.4. Boundary condition for intermediate velocity

As shown in Section 2.3.3, we use a fractional-step method with a semi-implicit scheme for the viscous terms. A boundary condition for the intermediate velocity $(\hat{u}, \hat{v}, \hat{w})$ is thus needed. By substituting Eq. (30) into Eqs. (18)–(20), we obtain the following free-surface boundary conditions:

$$\frac{\partial \hat{u}}{\partial \zeta} = S_u^1 + S_\wp^1 + S_f^1 \quad \text{at } z = \eta, \tag{37}$$

$$\frac{\partial \hat{v}}{\partial \zeta} = S_u^2 + S_\wp^2 + S_f^2 \quad \text{at } z = \eta, \tag{38}$$

$$\frac{\partial \hat{w}}{\partial \zeta} = S_u^3 + S_\wp^3 \quad \text{at } z = \eta, \tag{39}$$

where for $i = 1, 2$

$$S_u^i = C_0\left\{C_1^i\left(\frac{\partial \hat{u}}{\partial \varphi} + \frac{\partial \hat{v}}{\partial \xi}\right) + C_2^i\frac{\partial \hat{u}}{\partial \xi} + C_3^i\frac{\partial \hat{v}}{\partial \varphi} + C_4^i\frac{\partial \hat{w}}{\partial \xi} + C_5^i\frac{\partial \hat{w}}{\partial \varphi}\right\}, \tag{40}$$

$$S_\wp^i = -C_0\frac{\Delta t}{\rho}\left\{C_1^i\left[\frac{\partial}{\partial \varphi}\left(\frac{\partial \wp}{\partial \xi} + \zeta_x\frac{\partial \wp}{\partial \zeta}\right) + \frac{\partial}{\partial \xi}\left(\frac{\partial \wp}{\partial \varphi} + \zeta_y\frac{\partial \wp}{\partial \zeta}\right)\right]^{(n+1)} + C_2^i\frac{\partial}{\partial \xi}\left(\frac{\partial \wp}{\partial \xi} + \zeta_x\frac{\partial \wp}{\partial \zeta}\right)^{(n+1)} + C_3^i\frac{\partial}{\partial \varphi}\left(\frac{\partial \wp}{\partial \varphi} + \zeta_y\frac{\partial \wp}{\partial \zeta}\right)^{(n+1)}$$
$$+ C_4^i\frac{\partial}{\partial \xi}\left(\zeta_z\frac{\partial \wp}{\partial \zeta}\right)^{(n+1)} + C_5^i\frac{\partial}{\partial \varphi}\left(\zeta_z\frac{\partial \wp}{\partial \zeta}\right)^{(n+1)}\right\} + \frac{\Delta t}{\rho}\frac{\partial}{\partial \zeta}\left(\frac{\partial \wp}{\partial \xi_i} + \zeta_i\frac{\partial \wp}{\partial \zeta}\right)^{(n+1)}, \tag{41}$$

$$S_f^i = C_0\left(C_6^i\frac{\sigma_{t1}|_{external}}{\rho v} + C_7^i\frac{\sigma_{t2}|_{external}}{\rho v}\right), \tag{42}$$

and for $i = 3$

$$S_u^3 = -(\eta + H)\left(\frac{\partial \hat{u}}{\partial \xi} + \zeta_x S_u^1 + \frac{\partial \hat{v}}{\partial \varphi} + \zeta_y S_u^2\right), \tag{43}$$

$$S_\wp^3 = -\frac{\Delta t}{\rho}(\eta + H)\left\{-\frac{\partial}{\partial \xi}\left(\frac{\partial \wp}{\partial \xi} + \zeta_x\frac{\partial \wp}{\partial \zeta}\right)^{(n+1)} + \zeta_x S_\wp^1 - \frac{\partial}{\partial \varphi}\left(\frac{\partial \wp}{\partial \varphi} + \zeta_y\frac{\partial \wp}{\partial \zeta}\right)^{(n+1)} + \zeta_y S_\wp^2\right\} + \frac{\Delta t}{\rho}\frac{\partial}{\partial \zeta}\left(\zeta_z\frac{\partial \wp}{\partial \zeta}\right)^{(n+1)}. \tag{44}$$

Similarly, by substituting Eq. (30) into Eq. (24), we have the Dirichlet bottom boundary condition for velocity

$$
\begin{cases}
\hat{u} = u_b^{(n+1)} + \frac{\Delta t}{\rho}\left(\frac{\partial \wp}{\partial \xi} + \zeta_x \frac{\partial \wp}{\partial \zeta}\right)^{(n+1)} & \text{at } z = -H, \\
\hat{v} = v_b^{(n+1)} + \frac{\Delta t}{\rho}\left(\frac{\partial \wp}{\partial \varphi} + \zeta_y \frac{\partial \wp}{\partial \zeta}\right)^{(n+1)} & \text{at } z = -H, \\
\hat{w} = w_b^{(n+1)} + \frac{\Delta t}{\rho}\left(\zeta_z \frac{\partial \wp}{\partial \zeta}\right)^{(n+1)} & \text{at } z = -H.
\end{cases}
\tag{45}
$$

In Eqs. (41), (44) and (45), the value of $\wp^{(n+1)}$ is estimated by

$$
\wp^{(n+1)} = 3\wp^{(n)} - 3\wp^{(n-1)} + \wp^{(n-2)} + O(\Delta t^3).
\tag{46}
$$

Eq. (29) is solved subject to boundary conditions (37)–(39) and (45). Note that the right-hand sides of Eqs. (40) and (43) contain the unknown variables $(\hat{u}, \hat{v}, \hat{w})$, and iteration is thus required (see e.g. [53]). Typically two to four iterations are needed in our simulations for the relative residual error to be less than 10^{-10}.

As shown in Eq. (46), the information at the previous three timesteps is needed for the computation. Therefore, special treatment is needed for the self-starting of the scheme. We perform a preprocess simulation with a fine timestep of $\Delta t_0 = \Delta t/10$ for 30 timesteps, with the first three timesteps using forward Euler scheme. The values at $t = 0$, $10\Delta t_0$, and $20\Delta t_0$ are then used to start the formal simulation at $t = 30\Delta t_0$. With this treatment, our experience shows that the numerical error induced by the initial time integration is negligible.

2.3.5. Boundary condition and projection method for pseudo-pressure

In order to solve Eq. (36) for the pseudo-pressure $\wp$, proper boundary condition is needed. According to Eq. (34), the value of pseudo-pressure $\wp^{(n+1)}$ at $z = \eta$ is estimated as

$$
\wp^{(n+1)} = p^{(n+1/2)} + \frac{\rho \nu \Delta t}{2}\nabla^2 \wp^{(n+1)} = \frac{1}{8}\left(3p^{(n+1)} + 6p^{(n)} - p^{(n-1)}\right) + \frac{\rho \nu \Delta t}{2}\nabla^2\left(3\wp^{(n)} - 3\wp^{(n-1)} + \wp^{(n-2)}\right) + O(\Delta t^3).
\tag{47}
$$

The values of $p^{(n-1)}$, $p^{(n)}$ and $p^{(n+1)}$ are calculated by Eq. (17) based on $u_i^{(n-1)}$, $u_i^{(n)}$ and $u_i^{(n+1)}$, respectively. Here the value of $u_i^{(n+1)}$ is estimated using

$$
u_i^{(n+1)} = \hat{u}_i - \frac{\Delta t}{\rho}\frac{\partial}{\partial x_i}\left(3\wp^{(n)} - 3\wp^{(n-1)} + \wp^{(n-2)}\right) + O(\Delta t^3).
\tag{48}
$$

At the bottom boundary, a projection method is used [23] and a Neumann condition for $\wp^{(n+1)}$ is obtained from Eq. (30) as

$$
\frac{\partial \wp^{(n+1)}}{\partial \zeta} = \frac{\rho}{\Delta t \zeta_z}(\hat{w} - w_b^{(n+1)}) \quad \text{at } z = -H.
\tag{49}
$$

We remark that with the numerical schemes in Eqs. (46) and (48), Eqs. (33) and (35) are solved separately. The iteration between Eqs. (33) and (35), which is usually required when a semi-implicit scheme is used (see e.g. [53]), is therefore avoided and the computational cost is reduced.

2.3.6. Summary of the numerical scheme

The general free-surface and wavy wall flow problem considered in this study is simulated on the basis of the following procedure:

(i) Update the surface elevation from $\eta^{(n)}$ to $\eta^{(n+1)^*}$ based on Eqs. (25) and (26) and calculate the corresponding Jacobian matrix equation (4).
(ii) Solve $\hat{u}_i$ from Eq. (33) subject to boundary conditions (37)–(39) and (45).
(iii) Solve $\wp^{(n+1)^*}$ from Eq. (35) subject to boundary conditions (17) and (49).
(iv) Update velocity from $\hat{u}_i$ to $u_i^{(n+1)^*}$ based on Eq. (30).
(v) Update the free-surface elevation from $\eta^{(n+1)^*}$ to $\eta^{(n+1)}$ based on Eqs. (27) and (28) and calculate Eq. (4).
(vi) Repeat steps (ii)–(iv) and obtain $u_i^{(n+1)}$ and $\wp^{(n+1)}$.

Note that $f^{(n+1)^*}$ denotes the variable after the first step of the RK2 scheme and $f^{(n+1)}$ denotes the variable after the second step (see Section 2.3.2). After the foregoing steps (i)–(vi), the entire simulation advances from timestep (n) to $(n+1)$.

We also note that various numerical schemes (i.e. RK2, AB2, and CN) are involved in the temporal integration, which have different stability criteria. Use x-direction as an example. The RK2 scheme for the free surface KBC requires that $\Delta t < c_1 \Delta x/c$ with $c_1 < 2$ (c is the phase speed of the surface wave); the AB2 scheme for the nonlinear convective terms of the bulk flow requires that $\Delta t < c_2 \Delta x/u$ with $c_2 < 1$; and the CN scheme for the viscous terms requires that $\Delta t < c_3 \mathrm{Re}(\Delta x)^2$ with $c_3 < 1$. The combinations of these schemes give the stability criterion $\Delta t = \min(c_1 \Delta x/c, c_2 \Delta x/u, c_3 \mathrm{Re}(\Delta x)^2)$. For the simulations considered in the present study, we set $c_1 = c_2 = c_3 = c_0$ with c_0 in the range of 0.4–0.9, and all the three directions are considered.

2.4. Parallelization

The computational domain is decomposed in the y-direction and parallelized using Message Passing Interface (MPI). For the spectral method in the horizontal directions, two-dimensional matrix transpose is used when fast Fourier transform (FFT) is needed in the y-direction [12]. Satisfactory scalability in terms of speed-up, load balancing, and memory allocation has been obtained on supercomputers of Cray XT4 and SGI Altix ICE.

3. Test results

We systematically test the performance of the present method using simulations of laminar and turbulent flows interacting with free surfaces and wavy boundaries. The test cases are documented in this section.

3.1. Decaying vortex

First, we test our Navier–Stokes solver by simulating the problem of a two-dimensional decaying vortex, which has an analytical solution [21,53]. In the domain of $(0 \leqslant x \leqslant 2\pi, 0 \leqslant z \leqslant \pi/2)$, the solution is given by

$$\begin{cases} u(x,z,t) = -\cos x \sin z e^{-2t}, \\ w(x,z,t) = \sin x \cos z e^{-2t}, \\ p(x,z,t) = -0.25(\cos 2x + \cos 2z)e^{-4t}. \end{cases} \tag{50}$$

This analytical solution is also used to prescribe the Dirichlet boundary conditions on the domain boundaries.

For the hybrid spatial discretization scheme used in the present method, the error is dominated by the finite difference scheme in the vertical direction and an overall second-order spatial accuracy is expected. For the test of spatial convergence rate m, we use three different grid resolutions: (1) 64×160, (2) 64×80, and (3) 64×40. Here and hereafter, the grid in each direction is evenly spaced unless otherwise indicated. We thus have the vertical grid sizes of the three cases as $\Delta z_2 = 2\Delta z_1$ and $\Delta z_3 = 4\Delta z_1$. The timestep is chosen such that the Courant number equals 0.5. Let $\epsilon_{i,j}^s = \max |f(\Delta z_i) - f(\Delta z_j)|$, where $f(\Delta z_i)$ is the simulation result of variable using the grid resolution of Δz_i, we have

$$m = -\log_2 \left(\frac{\epsilon_{2,1}^s}{\epsilon_{3,2}^s} \right). \tag{51}$$

Table 1 lists the error and spatial convergence rate, which confirms the second-order accuracy.

For the time integration, the timestep in our simulation is constrained by the Courant number, and the contribution of the temporal discretization error to the total numerical error is smaller than that of the spatial error [17,33,53]. To test the temporal convergence rate n, we use three different timesteps: $\Delta t_1 = 0.008$, $\Delta t_2 = 0.01$, and $\Delta t_3 = 0.012$. A reference simulation with $\Delta t_4 = 0.0008$ is also performed. All of the simulations are performed on a fixed 64×50 grid. The difference between each simulation and the reference case is used to eliminate the spatial discretization error [1,53]. Let $\epsilon_{i,j}^t = \max |f(\Delta t_i) - f(\Delta t_j)|$, we have

$$n = \frac{1}{2} \left\{ \log_{1.25} \left(\frac{\epsilon_{2,4}^t}{\epsilon_{1,4}^t} \right) + \log_{1.2} \left(\frac{\epsilon_{3,4}^t}{\epsilon_{2,4}^t} \right) \right\}. \tag{52}$$

As shown in Table 2, second-order temporal accuracy is obtained.

3.2. Flow over a stationary wavy wall

Next we perform tests for the problem of flow over a stationary wavy wall, for which data from previous studies exist for comparison. For all of our test cases in this subsection, a Couette flow driven by a constant shear stress at the top boundary that is kept flat is simulated; the bottom wavy boundary has the configuration matching those in the literature as discussed below.

Table 1
Convergence test of the decaying vortex case for different spatial resolutions with a fixed Courant number of 0.5. Result at $t = 0.24$ is used.

	Grid resolution (1) 64×160 (2) 64×80 (3) 64×40		Convergence rate m
u	$\epsilon_{2,1}^s = 3.1e-5$	$\epsilon_{3,2}^s = 1.2e-4$	2.0
w	$\epsilon_{2,1}^s = 5.2e-5$	$\epsilon_{3,2}^s = 2.1e-4$	2.0

Table 2
Convergence test of the decaying vortex case for different timesteps with a fixed spatial resolution 64×50. $\Delta t_4 = 0.0008$. Result at $t = 0.24$ is used.

	$\Delta t_1 = 0.008$	$\Delta t_2 = 0.01$	$\Delta t_3 = 0.012$	Convergence rate n
u	$\epsilon^t_{1,4} = 1.4e - 6$	$\epsilon^t_{2,4} = 2.3e - 6$	$\epsilon^t_{3,4} = 3.3e - 6$	2.1
w	$\epsilon^t_{1,4} = 6.9e - 7$	$\epsilon^t_{2,4} = 1.1e - 6$	$\epsilon^t_{3,4} = 1.6e - 6$	2.1

We first consider a two-dimensional laminar Couette flow, which was previously studied theoretically (see e.g. [4]) and numerically (see e.g. [43]). Our simulations are carried out with $\text{Re} = U\lambda/v = 10^4$ (U is the mean velocity at the top boundary, and λ is the wavelength of the wavy boundary) in a computational domain of size $(L_x, \overline{H}) = (\lambda, \lambda)$ using a 128×129 grid. The grid is clustered in the z-direction, with $\Delta z_{min} = 0.001\lambda$ near the bottom and top boundaries and $\Delta z_{max} = 0.015\lambda$ at the center of the domain. We remark that in this two-dimensional Couette flow case, the flow field is initially laminar and no turbulent disturbance is introduced in the simulation. With $\text{Re} = 10^4$, the flow remains laminar [43] and the result can be compared with the theoretical solution [4].

Fig. 3(a) and (b) shows the comparison of the surface pressure distribution with [4,43]. Both [4,43] used the same conformal-mapping-based boundary-fitted grid, with the former solving the Orr–Sommerfeld equation and the latter performing DNS of the Navier–Stokes equations. As shown in Fig. 3(a), for the case of small wave steepness $ak = 0.01$ (a is the wave amplitude and $k = 2\pi/\lambda$ is the wavenumber), the present result agrees well with the literature. Fig. 3(b) shows that, when the wave steepness increases to $ak = 0.2$, the present simulation on the non-orthogonal grid still provides the surface pressure that agrees well with the orthogonal-grid simulation result of [43]. At such large ak, the deviation from the linear theory of [4] is noticeable and is as expected.

We next test three-dimensional turbulent Couette flows. In our simulations, the Reynolds number is $\text{Re} = U\lambda/v = 10^4$; the computational domain has the size of $(L_x, L_y, \overline{H}) = (4\lambda, 3\lambda, 2\lambda)$; and the grid resolution is $128 \times 128 \times 129$ and is clustered in the vertical direction towards the boundary, with $\Delta z_{min} = 0.0015\lambda$ and $\Delta z_{max} = 0.03\lambda$. The turbulence is initially seeded by random velocity noises and then produced by the shear in the flow.

Fig. 4 shows the phase-averaged mean pressure distribution over a wavy boundary of $ak = 0.05\pi$, which matches the condition in [10,64]. Our result agrees with the DNS result of [10] and the laboratory measurement of [64]. The surface pressure is high on the windward face of the wavy surface, and is low around the crest and the leeward face, resulting in a form drag [3].

We next examine the statistics of the turbulence velocity fluctuations and the Reynolds stress. We denote the phase average of a quantity f as $\langle f \rangle$, and its fluctuation as $f' = f - \langle f \rangle$. We consider a wavy boundary of $ak = 0.1\pi$, which is close to the measurement condition of Hudson et al. [22]. As shown in Fig. 5(a), the Reynolds stress $\langle -u'w' \rangle$ is high above the wave
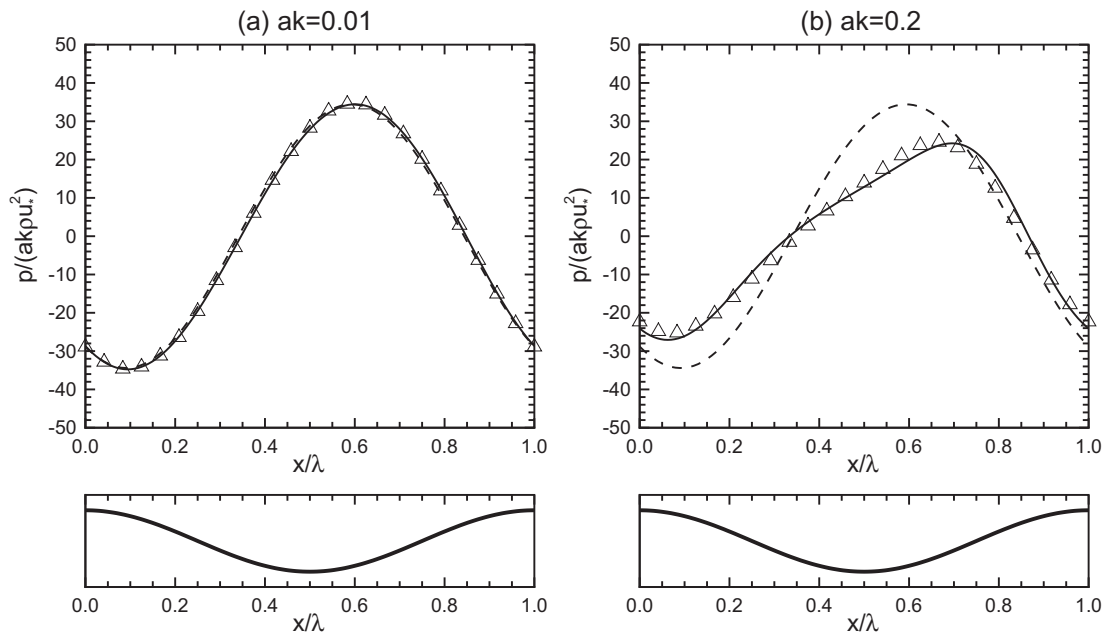
Fig. 3. Surface pressure distribution in flow over a stationary wavy wall. In (a) and (b), the case of laminar flow over wavy wall with steepness $ak = 0.01$ and 0.2 are plotted, respectively: —, current DNS result; – – –, prediction of the linear theory by Benjamin [4]; and △, DNS result by Sullivan et al. [43]. In each case, the phase of the wavy wall is indicated by the thick solid line at the bottom.
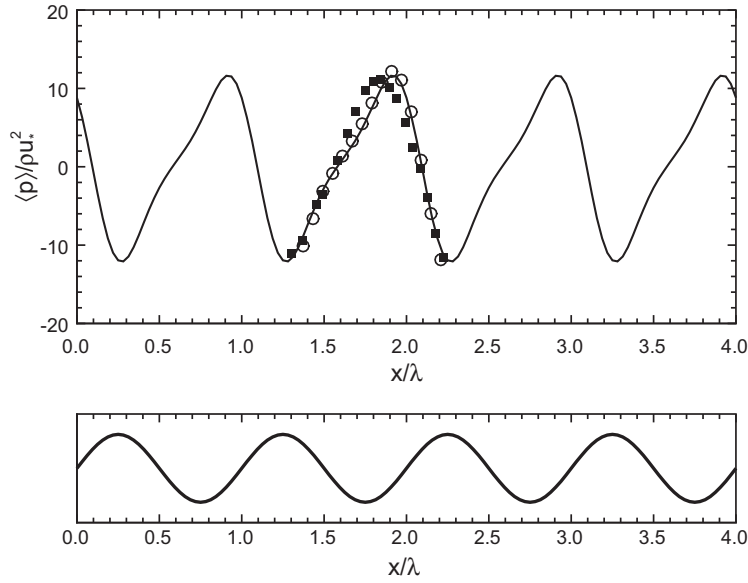
Fig. 4. Surface pressure distribution in turbulent flow over a stationary wavy wall with steepness $ak = 0.05\pi$: —, current DNS result; ○, DNS result by De Angelis et al. [10]; and ■, experiment data by Zilker et al. [64]. The phase of the wavy wall is indicated by the thick solid line at the bottom.

trough, but has small negative values on the windward face of the wave crest. Associated with the high Reynolds stress, the root-mean-square (rms) value of the streamwise velocity fluctuation, u'_{rms}, is also high above the wave trough (Fig. 5(b)). Fig. 5(c) shows that the value of w'_{rms} reaches its maximum value above the windward face of the crest. The wave-coherent distributions of turbulence statistics obtained in the present study agree with the measurement data of [22] (see their Figs. 6 and 9). For example, they showed that the Reynolds stress has a maximum value of 1.66 around $(x,z)/\lambda = (0.53, 0.05)$ and a minimum value of about -0.2 on the windward face, and in the present study the maximum is 1.64 at $(x,z)/\lambda = (0.56, 0.05)$ and a minimum value of -0.3 on the windward face (Fig. 5(a)). The value and location for the maximum u'_{rms} and w'_{rms} obtained from the present simulation also agree with those from [22] (Fig. 5(b) and (c)).

3.3. Surface waves

3.3.1. Comparison with theoretical two-dimensional wave solutions

In this subsection, theoretical solutions for three types of two-dimensional water waves are used to test the free surface simulation capability of the present method. The simulation of linear viscous wave provides a test for the viscous terms in Eqs. (17)–(20); the capillary wave case tests the surface tension condition in Eq. (17); and the Stokes wave case tests the nonlinear KBC and DBC.

In this subsection, we use a to denote wave amplitude, λ for wavelength, $k = 2\pi/\lambda$ for wavenumber, T for wave period, $\omega = 2\pi/T$ for angular frequency, and c for wave phase speed. For all of the test cases here, we set λ to be 2π and the size of the computational domain to be $(L_x, \overline{H}) = (2\pi, 3.5)$. Since $\overline{H} > \lambda/2$, the deep water condition is satisfied.

(i) Linear viscous wave:
From Lamb [25], we consider a linear wave with viscous effect:

$$\begin{cases} \eta(x,z,t) = a_0 \exp\left(-2\nu k^2 t\right) \sin(kx + \omega t), \\ u_\phi(x,z,t) = -\omega a_0 \exp\left(kz - 2\nu k^2 t\right) \sin(kx + \omega t), \\ w_\phi(x,z,t) = \omega a_0 \exp\left(kz - 2\nu k^2 t\right) \cos(kx + \omega t), \\ u_\nu(x,z,t) = 2\nu k\beta a_0 \exp\left(\beta z - 2\nu k^2 t\right)[\sin(kx + \beta z + \omega t) \\ \qquad\qquad - \cos(kx + \beta z + \omega t)], \\ w_\nu(x,z,t) = -2\nu k^2 a_0 \exp\left(\beta z - 2\nu k^2 t\right) \sin(kx + \beta z + \omega t), \end{cases} \qquad (53)$$

where (u_ϕ, w_ϕ) and (u_ν, w_ν) are respectively the potential and viscous parts of the wave orbital velocity; and $\beta = \sqrt{\omega/2\nu}$ is the depth dependence coefficient for the viscous part of the velocity. The dispersion relationship gives
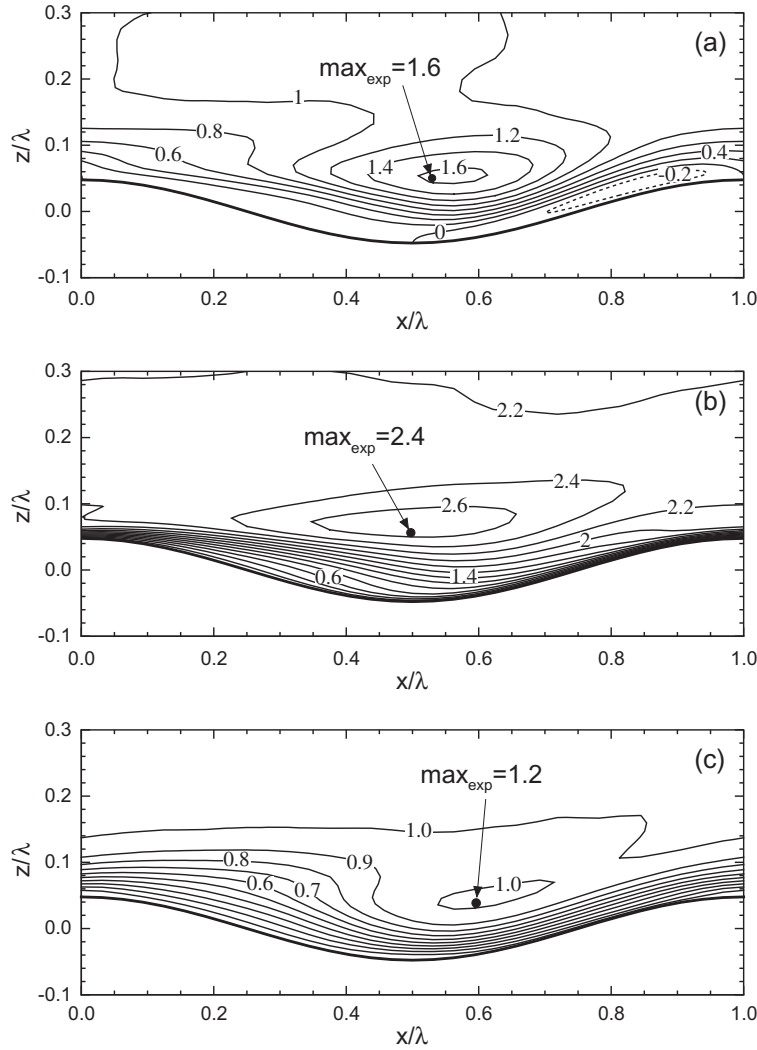
Fig. 5. Turbulence statistics in flow over stationary wavy wall with steepness $ak = 0.1\pi$: (a) Reynolds stress, $\langle -u'w' \rangle$; (b) root-mean-square value of streamwise velocity fluctuation, u'_{rms}; and (c) root-mean-square value of vertical velocity fluctuation, w'_{rms}. For each quantity, the corresponding maximum value obtained in the experiment of Hudson et al. [22], $\max_{exp}$, is given in the figure and its location is indicated by $\bullet$.

$\omega = \sqrt{gk + \gamma k^3}$. We choose $a_0 k = 0.01$, $\mathrm{Fr}^2 = c^2/(g/k) = 1$, $\mathrm{We} = (\rho c^2/k)/\gamma = \infty$, and $\mathrm{Re} = (c/k)/\nu = 500$. For comparison, an additional case with $\mathrm{Re} = 50$ is also studied.

(ii) Capillary wave:

We test capillary waves based on Crapper's solution [8]. In the frame traveling with the wave phase speed, the general form of Crapper's wave is

$$
\begin{cases}
\frac{x}{\lambda} = \frac{\phi}{c\lambda} - \frac{2}{\pi} \frac{A e^{-2\pi\psi/c\lambda} \sin(2\pi\phi/c\lambda)}{1 + A^2 e^{-4\pi\psi/c\lambda} + 2A e^{-2\pi\psi/c\lambda} \cos(2\pi\phi/c\lambda)}, \\
\frac{y}{\lambda} = \frac{\psi}{c\lambda} - \frac{2}{\pi} \frac{1 + A e^{-2\pi\psi/c\lambda} \cos(2\pi\phi/c\lambda)}{1 + A^2 e^{-4\pi\psi/c\lambda} + 2A e^{-2\pi\psi/c\lambda} \cos(2\pi\phi/c\lambda)}.
\end{cases}
\tag{54}
$$

Here, ϕ and ψ are the potential function and the stream function of the wave, respectively; $A = 4 \left(\sqrt{1 + (ak)^2/16} - 1 \right) \Big/ (ak)$; and the wave phase speed satisfies $c = \sqrt{k\gamma/\rho} \sqrt{(1 - A^2)/(1 + A^2)}$. The surface elevation is obtained by substituting $\psi = 0$ into the above general formula. The $\phi(x,z)$ and $\psi(x,z)$ are then solved by using the Newton–Raphson iteration. Velocity is calculated as $(u, w) = (\partial\phi/\partial x, \partial\phi/\partial z)$. We choose $ak = 0.1$, $\mathrm{Fr}^2 = c^2/(g/k) = \infty$, $\mathrm{We} = (\rho c^2/k)/\gamma = 1$, and $\mathrm{Re} = (c/k)/\nu = 3162$.

(iii) High-order Stokes wave:
We consider the Stokes wave [41], for which the solution was extended to high order by Schwartz [37] using computer calculation. In the present study, by following [14], we directly solve the nonlinear equations associated with the mapping function in [37] (see their Eq. (2.6)) by using Newton iteration. We choose $ak = 0.1, \mathrm{Fr}^2 = c^2/(g/k) = 1, \mathrm{We} = (\rho c^2/k)/\gamma = \infty$, and $\mathrm{Re} = (c/k)/v = 500$.

Figs. 6 and 7 show the test results of the above three wave cases. Fig. 6 shows the evolution of the amplitude of the linear viscous wave. Because of the viscous dissipation, the wave decays in time. For $\mathrm{Re} = 500$, our simulation result agrees well with the theory of [25] (Eq. 53). When the Reynolds number reduces to $\mathrm{Re} = 50$, the wave decays faster than that for $\mathrm{Re} = 500$, and the current simulation result agrees with Eq. (53) but with small difference, which is as expected because in [25] it is assumed $\mathrm{Re} \gg 1$.

Fig. 7(a) shows the surface profiles of the capillary wave and the Stokes wave. For $ak = 0.1$, the wave nonlinearity is non-negligible. For the capillary wave, the wave trough is sharper than the crest [8]; on the contrary, for the Stokes wave the crest is sharper than the trough [25]. The wave profiles obtained by the present method agree well with the theoretical solutions for both the capillary and Stokes waves, which can also be seen from the small difference between the simulation results and the theoretical solutions shown in Fig. 7(b).

Similar to Section 3.1, we also perform convergence test for the above three water wave cases. We choose three different grid resolutions: $32 \times 160, \ 32 \times 80$, and 32×40. We calculate the numerical error in the surface elevation η. Table 3 shows the error and convergence rate. For all the wave cases, second-order accuracy is obtained by the present method.

We remark that the present scheme is for flows with moderate surface deformation. Although an overall second order scheme is used, increasing the amplitude or the propagation speed of the surface deformation would usually lead to a decreased accuracy in the global solver. For example, our numerical experience shows that the order of accuracy reduces to about 1.5 if the wave steepness exceeds $ak = 0.25$. For $ak < 0.2$, a second order accuracy can be obtained.

3.3.2. Comparison with crescent wave results

Next, we test the present method using the problem of crescent wave, which is generated from an initially disturbed Stokes wave due to nonlinear wave interaction and free surface instability. Such processes pose a great challenge to the numerical simulation in terms of the accuracy of free surface treatment [50]. We consider the L_2 type instability [27]. Our simulation starts with a plane-progressive Stokes wave, which has amplitude a, wavenumber k, and crest located at $x = 0$ at $t = 0$. Initially a three-dimensional perturbation is introduced with the surface elevation η^* and velocity potential ϕ^* given as [27,51]

$$\begin{cases} \eta^* = \epsilon a \sin k_x x \cos k_y y, \\ \phi^* = -\frac{\epsilon a}{(k_x^2+k_y^2)^{1/4}} \cos k_x x \cos k_y y \exp[(k_x^2 + k_y^2)^{1/2} z]. \end{cases} \tag{55}$$

Here, ϵ measures the amplitude of the perturbation; $(k_x, k_y) = (k + m, n)$, where m and n are the streamwise and spanwise perturbation wavenumbers.

We match the simulation parameters with those in [51]. We set $k = 1$ and $a = 0.33$ for the Stokes wave. For the initial perturbation, we set $\epsilon = 0.16, \ m = 0.5$, and $n = 1.23$. We choose $\mathrm{Fr}^2 = c^2/(g/k) = 1, \mathrm{We} = (\rho c^2/k)/\gamma = \infty$, and $\mathrm{Re} = (c/k)/v = 1000$. A computational domain of size $(L_x, L_y, \overline{H}) = (4\pi, 4\pi/1.23, 2\pi)$ with a $128 \times 128 \times 97$ grid is used. The grid is clustered in the z-direction, with $\Delta z_{min} = 0.026$ near the free surface and $\Delta z_{max} = 0.1$ in the bulk flow.
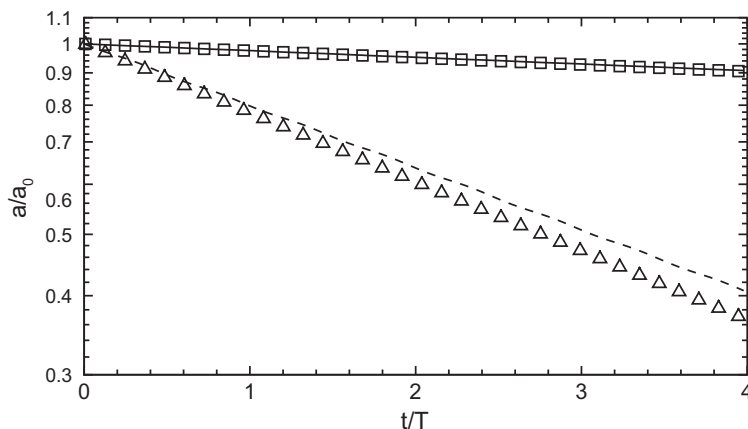
Fig. 6. Decay of the linear viscous wave. For $\mathrm{Re} = 500$: —, current DNS result; □, theoretical prediction by Eq. (53). For $\mathrm{Re} = 50$: – – –, current DNS result; △, theoretical prediction by Eq. (53). Here a_0 is the initial wave amplitude. The vertical axis is plotted in logarithmic scale.
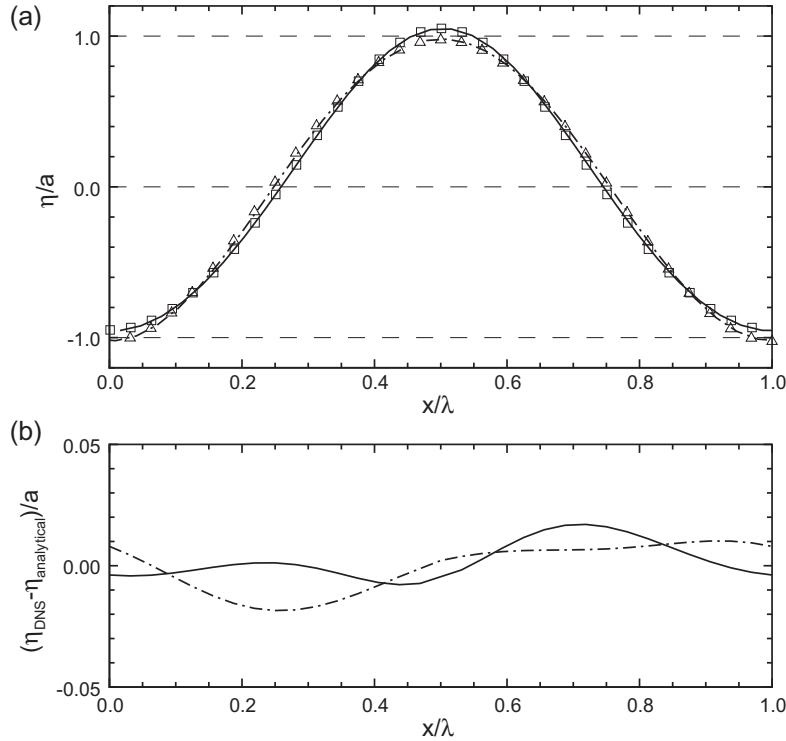
Fig. 7. (a) Surface profiles of capillary wave and Stokes wave. For capillary wave: $-\cdot-$, current DNS result at $t = 6T$; $\triangle$, analytical solution by Crapper [8]. For Stokes wave: $-$, current DNS result at $t = 6T$; $\square$, analytical solution by Schwartz [37]. (b) Difference between the current DNS result and the analytical solution: $-\cdot-$, capillary wave; and $-$, Stokes wave.

Table 3
Convergence tests of various waves for different spatial resolutions with a fixed Courant number of 0.5.

| Wave type	Grid resolution (1) 32×160 (2) 32×80 (3) 32×40		Convergence rate m
Linear viscous wave	$\epsilon^s_{2,1} = 2.2e - 5$	$\epsilon^s_{3,2} = 7.8e - 5$	1.8
Capillary wave	$\epsilon^s_{2,1} = 1.1e - 3$	$\epsilon^s_{3,2} = 5.5e - 3$	2.3
Stokes wave	$\epsilon^s_{2,1} = 3.4e - 3$	$\epsilon^s_{3,2} = 1.5e - 2$	2.2

Fig. 8 shows the nonlinear development of the L_2 type crescent wave. Initially, the surface is close to the Stokes wave shape with small perturbations at the crests (Fig. 8(a)). At $t = 3.17T$ (where T is the period of the Stokes wave), the crests become sharper and the crescent shape of the waves is observed (Fig. 8(b)). For $t > 4T$, as the edges of the crescent lines extend more in the $-x$-direction and the crests become steeper, the semi-circular sharp crescent crests are well-formed (Fig. 8(c) and (d)). The above development process agrees well with the result of the mixed-Eulerian–Lagrangian (MEL) simulation based on the high-order boundary-element method presented in Ref. [51] (as shown in their Fig. 11).

Fig. 9 shows the surface elevation contours at $t = 4.34T$. The spanwise shift of the crescents on successive wave crests [42], which are thus staggered, is shown clearly. For example, at $x \approx 2$, the center of the crescent is located at $y = \pm 2.55$ (i.e. half-width of the perturbation); at $x \approx 9$, the center of the crescent shifts to $y = 0$ and ± 5.11.

Fig. 10 shows the streamwise surface profile along $y = 0$ at $t = 4.34T$. As a result of the crescent shift, the wave crest at $x \approx 2$ is apparently lower than that at $x \approx 9$. Comparison shows that our simulation result agrees well with previous experimental, theoretical, and numerical studies [27,42,51].

3.4. Interaction of vortex pair with free surface

Next, we examine the interaction of vortices with the free surface. We consider a two-dimensional vortex pair raising to the free surface [2,32]. We use a computational domain of size $(L_x, \overline{H}) = (6.0, 6.0)$. A pair of counter-rotating vortices are initially located at $(x_0, z_0) = (\pm l_0/2, -h_0) = (\pm 0.5, -3.0)$ (where l_0 is the distance between the vortex cores, and h_0 is their depth under the undisturbed free surface), with the circulation $\Gamma_0 = 1.0$ and the radius of vortex core $r_0 = 0.25$. The initial flow field is created using a Lamb vortex solution inside the vortex core and the potential flow solution outside [32].
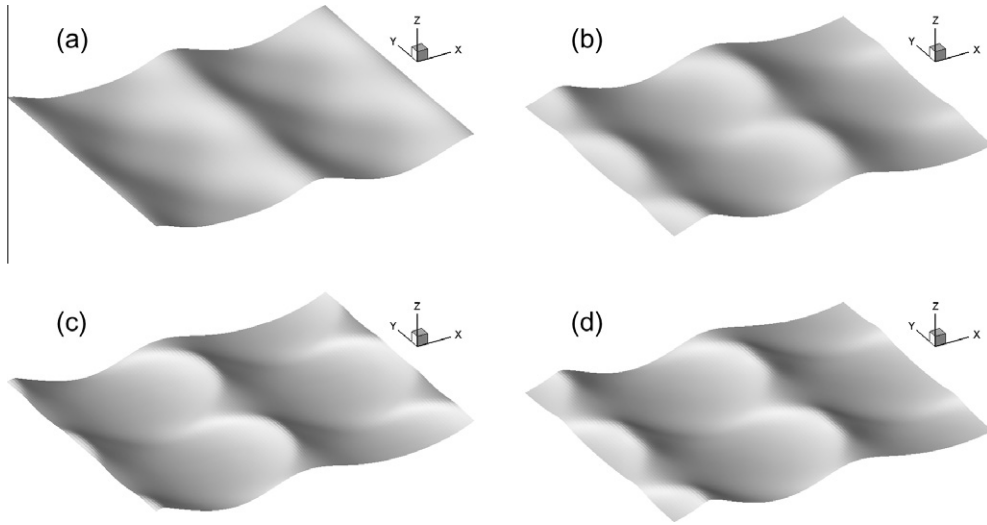
Fig. 8. Free-surface pattern during the nonlinear development of crescent wave from disturbed steep Stokes wave at $t/T =$ (a) 0, (b) 3.17, (c) 4.96, and (d) 5.15. Here T is the period of the original Stokes wave.
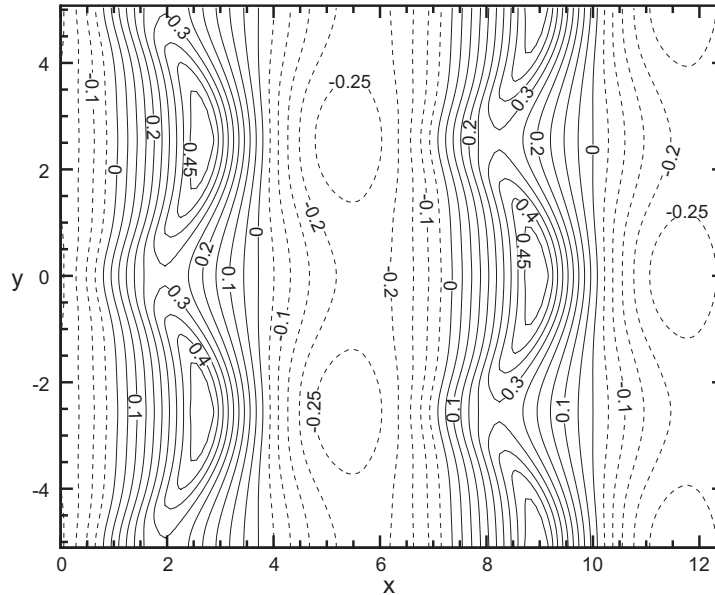

Fig. 9. Surface elevation contours of the crescent wave at $t/T = 4.34$. Here T is the period of the original Stokes wave. The dashed contour lines represent negative values.

We set $Fr^2 = \Gamma_0^2/(gl_0^3) = 0.02$, $Re = \Gamma_0/\nu = 100$, and $We = (\rho\Gamma_0^2)/(\gamma l_0) = \infty$. We use a grid resolution with 128 points in the horizontal direction. In the vertical direction, the grid is clustered near the free surface; two grids of $Nz = 129$ and 65 are used for comparison. For $Nz = 129$, the minimum and maximum vertical grid sizes are $\Delta z_{min} = 0.004$ and $\Delta z_{max} = 0.084$, respectively; for $Nz = 65$, we have $\Delta z_{min} = 0.009$ and $\Delta z_{max} = 0.168$. The timestep is $\Delta t = 0.0025$.

The method developed in [62] (referred to as Z96) is used for comparison, which also employs a boundary-fitted grid with fully nonlinear free-surface KBC and DBC. In Z96, a pseudo-spectral method and a second-order finite difference scheme are used in the horizontal and vertical directions, respectively. The simulation is advanced in time by a second-order Runge–Kutta scheme that is explicit (while in the present method, we treat the viscous terms semi-implicitly). The grids are evenly distributed in both the horizontal and vertical directions (while in the present method, the grid is clustered vertically). Because Z96 uses equidistant grid in the z-direction, more grid points are needed to resolve the surface boundary layer. We use $Nz = 513$ and 129 for comparison, which correspond to $\Delta z = 0.012$ and 0.047, respectively. A smaller timestep $\Delta t = 0.001$ is needed for Z96.

Fig. 11 shows the results. Due to the symmetry of the problem, only half of the domain ($x > 0$) is plotted. When the vortex pair approaches the surface, the surface between the vortices is pushed up by the upwelling flow; meanwhile, the surface on the two sides is rolled down, with surface vortices generated [2]. With the fine vertical grid resolutions, the results of the present method and Z96 agree with each other, and the primary and secondary surface vortices are resolved in both cases
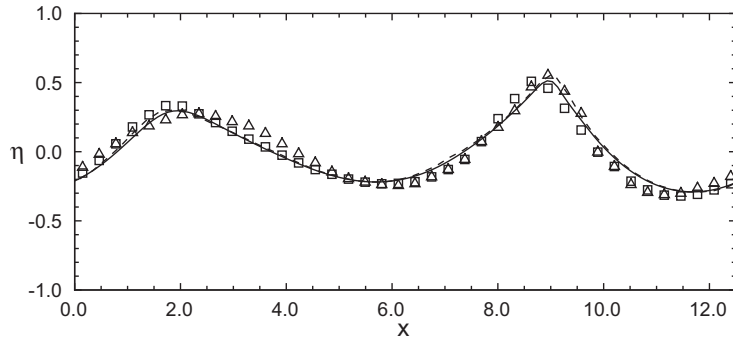
Fig. 10. Streamwise profile of the L_2 crescent wave on the plane $y = 0$ at $t/T = 4.34$: △, experimental data of Su [42]; □, result by the perturbation method [27]; – – –, numerical result by the MEL method [51]; and —, the current DNS result.
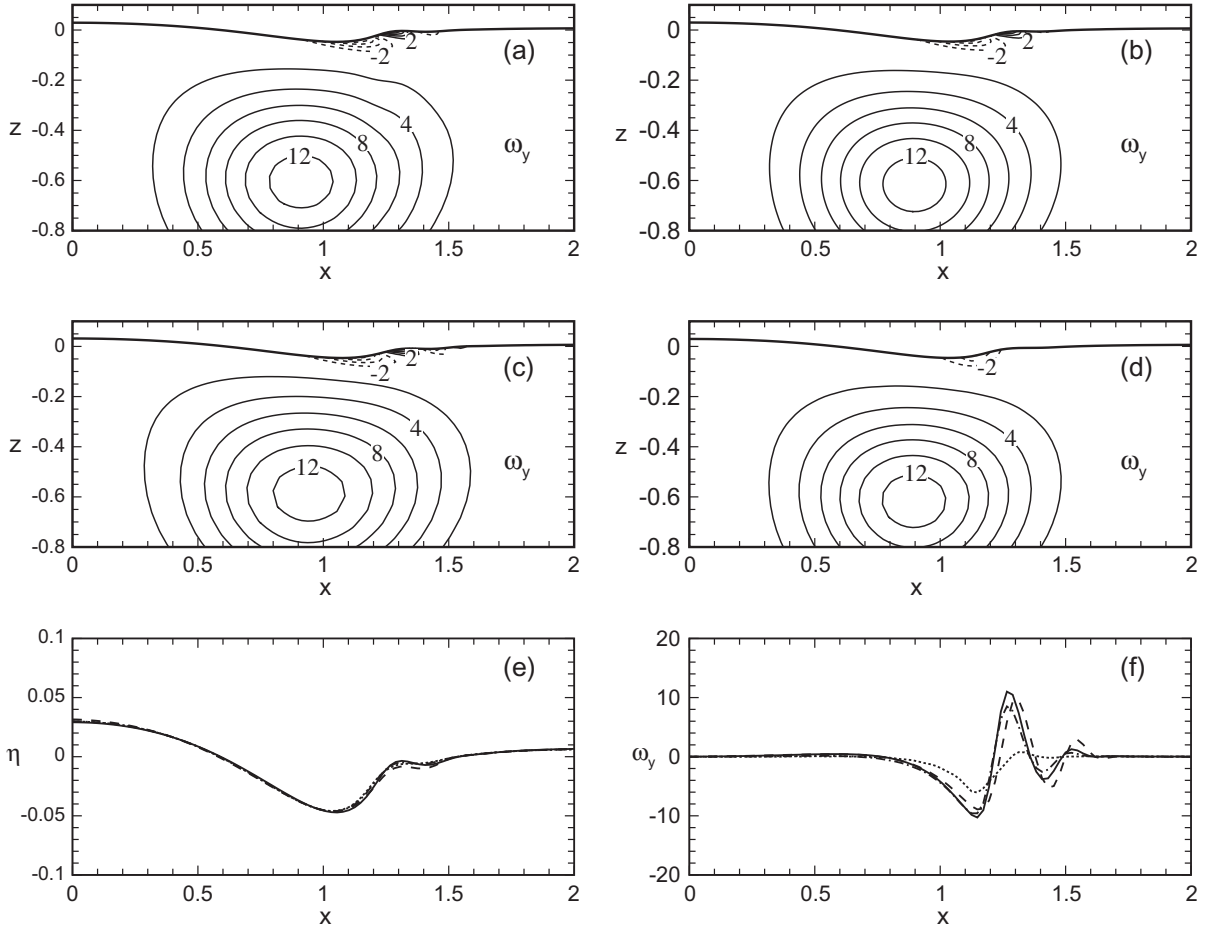
Fig. 11. Interaction of a vortex pair with free surface. Due to the symmetry of the problem, only half of the domain ($x > 0$) is plotted. Plotted in (a)–(d) are transverse vorticity ω_y at $t = 3.5$. Simulation results by the current method are compared with the result by the method of [62] (Z96) with various grid resolutions. Current method with clustered vertical grid: (a) $Nz = 129$ and (c) $Nz = 65$; and the Z96 method with evenly spaced vertical grid: (b) $Nz = 513$ and (d) $Nz = 129$. Plots (e) and (f) show respectively the surface elevation and transverse vorticity on the free surface in cases (a)–(d): (a) —; (b) – · –; (c) – – –; and (d) · · ·.

(Fig. 11(a) and (b)). When we reduce the grid number, the present method with $Nz = 65$ still captures the primary and secondary surface vortices (Fig. 11(c)), while Z96 with $Nz = 129$ captures only the primary surface vortex roughly (Fig. 11(d)).

Fig. 11(e) and (f) compares the profiles of surface elevation η and the surface value of transverse vorticity ω_y between the present method and Z96. The surface geometry is found to agree well for the grid resolutions considered. The surface distribution of ω_y is qualitatively consistent between the two methods; but the result of Z96 with $Nz = 129$ shows apparent deviation from other cases with much smaller magnitude.

The above test results indicate that the present method can resolve the near-surface flow structures adequately at relatively low computational cost compared with Z96. This feature is as expected because of the different treatment in the z-direction discretization.

3.5. Interaction of turbulence with free surface

Finally, we discuss the interaction of a deformable surface with turbulence. As a canonical problem, isotropic and homogeneous turbulence is generated by a linear forcing method in the bulk flow and is transported toward the free surface (see [18] for details). We use a computational domain of size $(L_x, L_y, \overline{H}) = (2\pi, 2\pi, 5\pi)$ and a $128 \times 128 \times 349$ grid. The grid is clustered in the z-direction with $\Delta z_{min} = 0.0025$ near the free surface and $\Delta z_{max} = 0.049$ in the bulk flow.

For the analysis of turbulence statistics in this subsection, we define $\tilde{z}$ as the signed distance from the free surface ($\tilde{z} < 0$ below the free surface) [19]. For a variable $f(x, y, z, t)$, its mean value $\bar{f}(\tilde{z})$ is defined as the average over the plane of constant $\tilde{z}$ and over time, and its fluctuation is obtained as $f' = f - \bar{f}$.

In the near surface region (at $\tilde{z} = -\pi/4$), the rms value of horizontal velocity fluctuations is $u'_{rms} = 0.090$ and the Taylor scale is $L_T = 0.339$. Based on u'_{rms} and L_T, we have $Re_T = u'_{rms} L_T / \nu = 30.39$, $Fr^2 = u'^2_{rms}/(gL_T) = 0.02$, and $We = \rho u'^2_{rms} L_T/\gamma = 0.11$. A snapshot of the simulation result is shown in Fig. 12.

Figs. 13–16 show the results. As turbulence eddies raise up, they distort the free surface and generate splats (upwellings), anti-splats (downwellings), dimples, and scars (see e.g. the review by Ref. [35]). Fig. 13 shows the effect of a splat on the deformation of the free surface. At the beginning of the splat event (Fig. 13(a)), the free surface is pushed up by the upwelling flow at the splat core. Due to the blockage effect of the surface, fluid particles diverge and travel along the surface radially (Fig. 13(b)). Some distance away, at the location where the radial velocity is maximum and the pressure is lowered, the surface is depressed to form a low-elevation ring (Fig. 13(c)). This ring-like wave propagates away from the splat when time goes on (Fig. 13(d) and (e)), with the wave amplitude decreasing because of dissipation and the spreading of wave energy over a larger annular area (Fig. 13(f)).
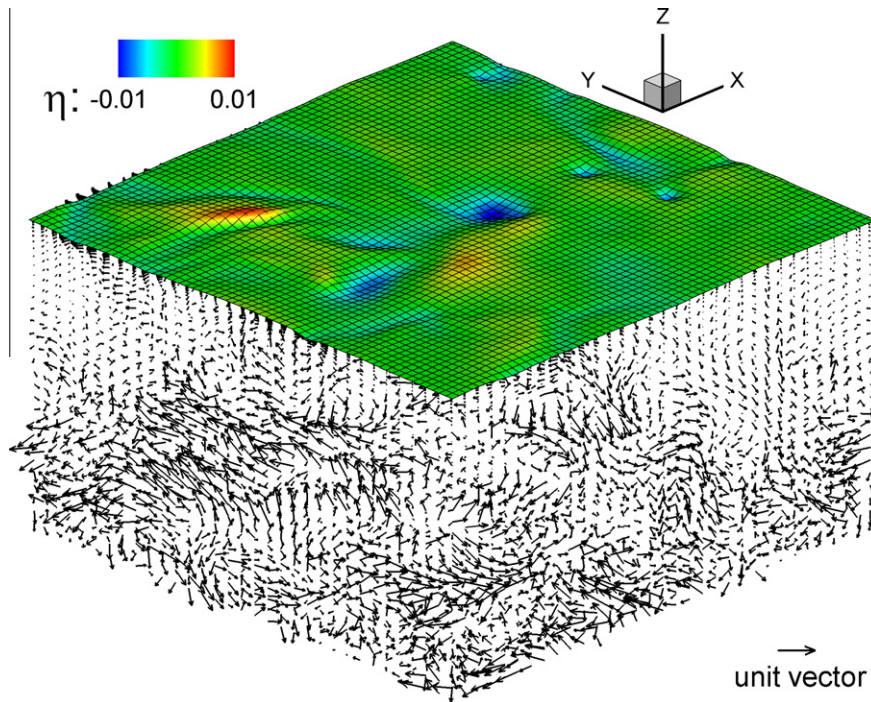
Fig. 12. Snapshot of a homogenous turbulence field underneath a free surface. Contours of surface elevation η is shown. Three-dimensional velocity vectors (u, v, w) are plotted in the bulk flow for every 4 grid points. Only the near-surface region of the computational domain is plotted.
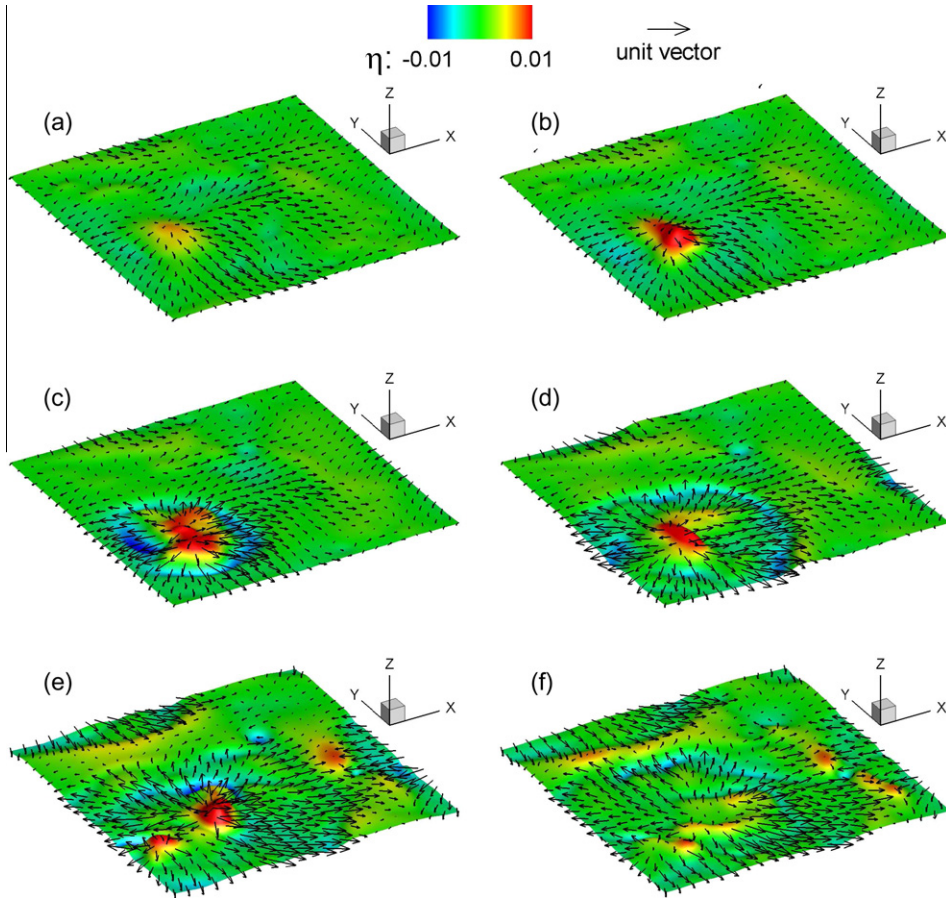
**Fig. 13.** Evolution of the free surface when a splat happens: (a) $t = 247$, (b) $t = 248$, (c) $t = 250$, (d) $t = 252$, (e) $t = 255$, and (f) $t = 257$. Contours of elevation η are plotted on the surface. The vectors of (u, v) are also plotted for every six grid points.

Different from wall-bounded turbulence, in free-surface turbulence there exist vortices that connect to the surface, e.g. vortices $O_1 - O_5$ in Fig. 14. Their connections to the surface are indicated by the surface dimples and the vortical motions of the fluids, as shown in Fig. 14(a). These surface-connected vortices are often located in the anti-splat regions, which are indicated by the negative surface divergence shown in Fig. 14(b). As shown in Fig. 14(c), these surface-connected vortices are perpendicular to the free surface and are mainly along the z-direction, resulting in the strong vertical vorticity ω_z at the free surface (Fig. 14(a)).

During the interaction of the aforementioned turbulence structures with the free surface, surface waves (e.g. the one propagates away from a splat shown in Fig. 13) and surface roughnesses (e.g. the dimples shown in Fig. 14) are formed. These surface features have different frequency–wavenumber characteristics. As shown in Fig. 15, the potential energy is concentrated on two ridges in the spectrum, one with relatively high frequency and the other with low frequency. The former coincides with the wave dispersion relationship (the dashed line in Fig. 15), and the latter is associated with the turbulence-induced surface roughness [19].

Fig. 16 shows the vertical profiles of the rms velocity and vorticity fluctuations. Near $\tilde{z} = 0$, the vertical motion w'_{rms} is restrained and kinetic energy is redistributed to the horizontal directions to increase u'_{rms} (Fig. 16(a)). Fig. 16(b) shows that towards the surface, $(\omega'_z)_{rms}$ decreases gradually. The value of $(\omega'_x)_{rms}$, on the other hand, remains high until $\tilde{z} \approx -0.1$. As $\tilde{z}$ further approaches zero, $(\omega'_x)_{rms}$ first decreases rapidly [49], reaches the minimum value of 0.2 at $\tilde{z} \approx -0.005$, and then increases to about 0.5 at $\tilde{z} = 0$ because of the horizontal vorticity generated by the curved surface (cf. Fig. 11). Fig. 16 shows that the present method resolves the near-surface variation of the profiles, which is important for the statistical study of free-surface turbulence. More analysis on the turbulence statistics near the surface is given [19].

The numerical capability demonstrated in this section, together with those shown in Sections 3.3.1 and 3.3.2, provides a useful tool for the study of the complex interaction between turbulent flows and surface waves. Fig. 17 shows such a simulation example, in which a surface wavefield interacts with a counter-propagating turbulent shear flow underneath it. The waves are distorted by the turbulence, and the turbulence is affected by the wave modulation. Simulation-based study of turbulence and surface wave interaction using the present method is a subject of our ongoing research and will be reported in the future.
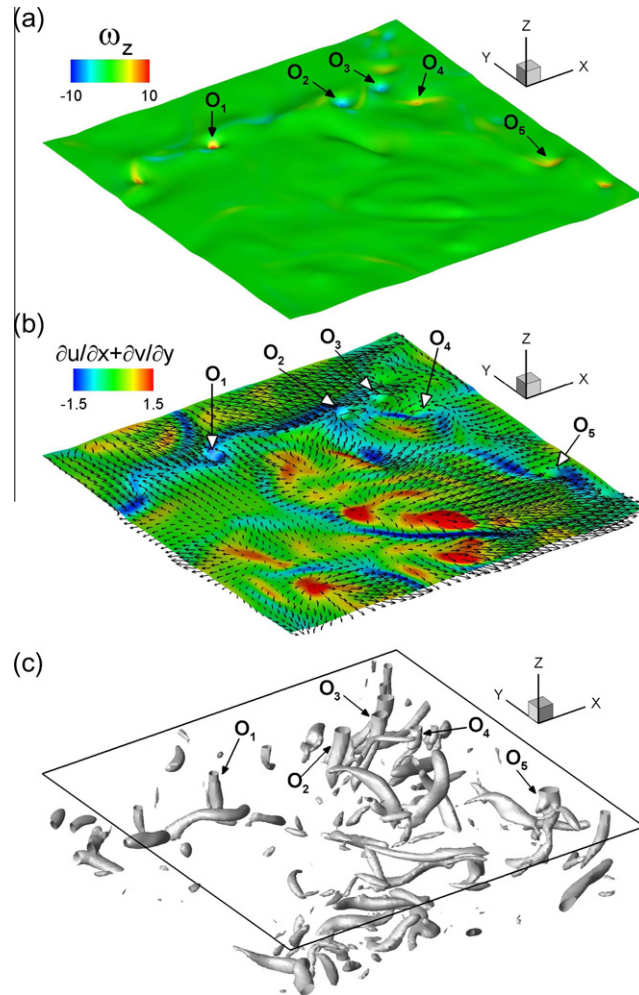
Fig. 14. Snapshot of instantaneous vortices near the free surface. The surface-connected vortices O_1–O_5 are indicated. Contours of the vertical vorticity ω_z and the surface divergence $\partial u/\partial x + \partial v/\partial y$ are plotted in (a) and (b), respectively. In (b), the velocity vectors (u, v) are also plotted for every four grid points. In (c), the vortices are represented by the iso-surface of $\lambda_2 = -1.2$. Here λ_2 is the second largest eigenvalue of the tensor $\mathbf{S}^2 + \mathbf{\Omega}^2$, where $\mathbf{S}$ and $\mathbf{\Omega}$ are respectively the symmetric and antisymmetric parts of the velocity gradient tensor $\nabla\mathbf{u}$.
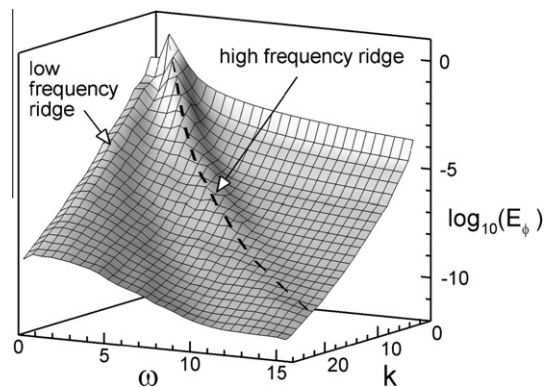
Fig. 15. Frequency–wavenumber spectrum E_ϕ of the surface elevation for the free surface interacting with homogeneous turbulence underneath it. The spectrum is normalized by $(\eta_{rms})^2$ and is shown on logarithm scale. The wave dispersion relationship is indicated by – – –.
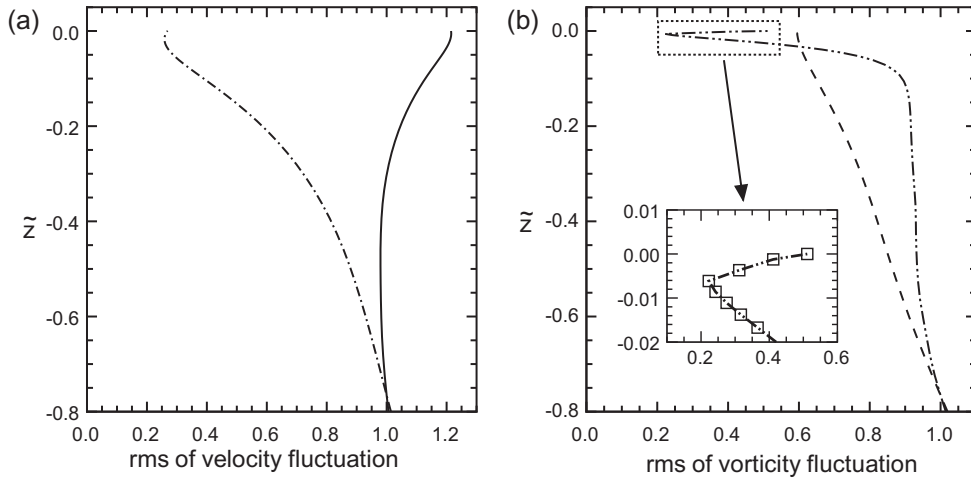
Fig. 16. Vertical profiles of (a) $(u_i')_{rms}/(u_i')_{rms}|_{\tilde{z}=-\pi/4}$ and (b) $(\omega_i')_{rms}/(\omega_i')_{rms}|_{\tilde{z}=-\pi/4}$ for the homogeneous turbulence underneath a free surface: —, u_{rms}'; – ·–, w_{rms}'; – ··–, $(\omega_x')_{rms}$; and – – –, $(\omega_z')_{rms}$.
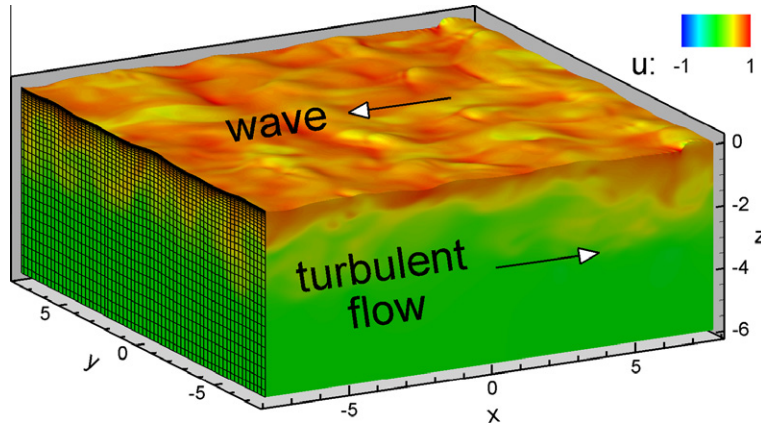
Fig. 17. Simulation result for the interaction of a surface wavefield with a counter-propagating turbulent shear flow underneath. Contours of the streamwise velocity are shown on the wave surface and the vertical planes. The vertically clustered computational grid is also plotted on the (y, z)-plane (for better visualization, the grid lines are plotted for every three grid points in both the horizontal and vertical directions).

4. Conclusions

In this paper, we present a numerical method for the simulation of laminar and turbulent flows with undulatory boundaries. A hybrid pseudo-spectral and finite difference scheme on a boundary-fitted grid is employed for spatial discretization. Fully nonlinear kinematic and dynamic boundary conditions are applied at the free surface. The three-dimensional Navier–Stokes equations are integrated in time by a fractional-step method with the boundary position tracked by a Runge–Kutta scheme. The pressure field is solved from a nonlinear Poisson equation.

In addition to the methodology development, special attention is paid to the validation and application of the present method. Extensive comparison with results in the literature is presented and the agreement is good. In particular, the simulations of flows with wavy boundaries and various surface waves validate the formulation and numerical implement of the kinematic and dynamic boundary conditions at the undulatory surfaces. Simulation of the crescent wave demonstrates the capability of the present method for capturing the nonlinear wave interaction and free surface instability. Comparison with Z96 [62] for the simulation of vortex and free surface interaction shows the accuracy of the present method for resolving near-surface flow structures.

Finally, the present method is applied to the problem of turbulence and free surface interaction. The result shows that both the instantaneous and the statistical features of the turbulence structures in the near-surface region are well resolved. The interaction between these structures and the free surface results in characteristic surface features including waves, splats, anti-splats, scars, and dimples. Direct observation and statistical analysis indicate that the present method adequately captures the details of the turbulence and free surface interaction.

The basic solver of viscous flows with undulatory boundaries presented in this paper provides a building block for the development of solvers for two-fluid computation with undulatory interface. In a companion paper [56], we discuss the coupling of the DNS discussed in this paper with potential flow based wave simulation for the study of wind–wave interaction, and the coupling of the DNS of one fluid with the DNS of another fluid for the study of interfacial viscous effects.

Acknowledgments

References

[1] K. Akselvoll, P. Moin, An efficient method for temporal integration of Navier–Stokes equations in confined axisymmetric geometries, J. Comput. Phys. 125 (1996) 454.
[2] P. Ananthakrishnan, R.W. Yeung, Nonlinear interaction of a vortex pair with clean and surfactant-covered free surfaces, Wave Motion 19 (1994) 343.
[3] S.E. Belcher, J.C.R. Hunt, Turbulent flow over hills and waves, Annu. Rev. Fluid Mech. 30 (1998) 507.
[4] T.B. Benjamin, Shearing flow over a wavy boundary, J. Fluid Mech. 6 (1959) 161.
[5] N. Bodard, R. Bouffanais, M.O. Deville, Solution of moving-boundary problems by the spectral element method, Appl. Numer. Math. 58 (2008) 968.
[6] R. Bouffanais, Simulation of shear-driven flows: transition with a free surface and confined turbulence, Ph.D. Thesis, Swiss Federal Institute of Technology, Schweizerische Nationalbibliothek NB 001515598, 2007.
[7] R. Bouffanais, M.O. Deville, Mesh update techniques for free-surface flow solvers using spectral element method, J. Sci. Comput. 27 (2006) 137.
[8] G.D. Crapper, An exact solution for progressive capillary waves of arbitrary amplitude, J. Fluid Mech. 2 (1957) 532.
[9] R.A. Dalrymple, P.L.F. Liu, Waves over soft muds: a two-layer fluid model, J. Phys. Oceanogr. 8 (1978) 1121.
[10] V. De Angelis, P. Lombardi, S. Banerjee, Direct numerical simulation of turbulent flow over a wavy wall, Phys. Fluids 9 (1997) 2429.
[11] A. Decoene, J.F. Gerbeau, Sigma transformation and ALE formulation for three-dimensional free surface flows, Int. J. Numer. Method Fluids 59 (2009) 357.
[12] P. Dmitruk, L.-P. Wang, W.H. Matthaeus, R. Zhang, D. Seckel, Scalable parallel FFT for spectral simulations on a Beowulf cluster, Parallel Comput. 27 (2001) 1921.
[13] D.G. Dommermuth, The laminar interactions of a pair of vortex tubes with a free surface, J. Fluid Mech. 246 (1993) 91.
[14] D.G. Dommermuth, D.K.P. Yue, A high-order spectral method for the study of nonlinear gravity waves, J. Fluid Mech. 184 (1987) 267.
[15] G.-J. Dong, X.-Y. Lu, Numerical analysis on the propulsive performance and vortex shedding of fish-like travelling wavy plate, Int. J. Numer. Methods Fluids 48 (2005) 1351.
[16] G.-J. Dong, X.-Y. Lu, Characteristics of flow over travelling wavy foils in a side-by-side arrangement, Phys. Fluids 19 (2007) 057107.
[17] J.H. Ferziger, M. Perić, Computational Methods for Fluid Dynamics, Springer, 2001.
[18] X. Guo, L. Shen, On the generation and maintenance of waves and turbulence in simulations of free-surface turbulence, J. Comput. Phys. 228 (2009) 7313.
[19] X. Guo, L. Shen, Interaction of a deformable free surface with statistically steady homogeneous turbulence, J. Fluid Mech. 658 (2010) 33.
[20] D.B. Haidvogel, H. Arango, W.P. Budgell, B.D. Cornuelle, E. Curchitser, E. Di Lorenzo, K. Fennel, W.R. Geyer, A.J. Hermann, L. Lanerolle, J. Levin, J.C. McWilliams, A.J. Miller, A.M. Moore, T.M. Powell, A.F. Shchepetkin, C.R. Sherwood, R.P. Signell, J.C. Warner, J. Wilkin, Ocean forecasting in terrain-following coordinates: formulation and skill assessment of the regional ocean modeling system, J. Comput. Phys. 227 (2008) 3595.
[21] R. Hodges, R.L. Street, On simulation of turbulent nonlinear free-surface flows, J. Comput. Phys. 151 (1999) 425.
[22] J.D. Hudson, L. Dykhno, T.J. Hanratty, Turbulence production in flow over a wavy wall, Exp. Fluids 20 (1996) 257.
[23] J. Kim, P. Moin, Application of a fractional-step method to incompressible Navier–Stokes equations, J. Comput. Phys. 59 (1985) 308.
[24] S. Komori, R. Nagaosa, Y. Murakami, S. Chiba, K. Ishii, K. Kuwahara, Direct numerical simulation of three-dimensional open-channel flow with zero-shear gas–liquid interface, Phys. Fluids A 5 (1993) 115.
[25] H. Lamb, Hydrodynamics, Dover, 1932.
[26] X.-Y. Lu, X.-Z. Yin, Propulsive performance of a fish-like travelling wavy wall, Acta Mech. 175 (2005) 197.
[27] J.W. McLean, Instabilities of finite-amplitude water waves, J. Fluid Mech. 114 (1982) 315.
[28] C.C. Mei, M. Krotov, Z. Huang, A. Huhe, Short and long waves over a muddy seabed, J. Fluid Mech. 643 (2010) 33.
[29] R. Mittal, S. Balachandar, Direct numerical simulation of flow past elliptic cylinders, J. Comput. Phys. 124 (1996) 351.
[30] R. Mittal, G. Iaccarino, Immersed boundary methods, Annu. Rev. Fluid Mech. 37 (2005) 239.
[31] P. Nielsen, O. Skovgaard, The effect of using non-orthogonal boundary-fitted grids for solving the shallow water equations, Int. J. Numer. Methods Fluids 11 (1990) 177.
[32] S. Ohring, H.J. Lugt, Interaction of a viscous vortex pair with a free surface, J. Fluid Mech. 227 (1991) 47.
[33] R.S. Rogallo, P. Moin, Numerical simulation of turbulent flows, Annu. Rev. Fluid Mech. 16 (1984) 99.
[34] S. Sankaranarayanan, M.L. Spaulding, A study of the effects of grid non-orthogonality on the solution of shallow water equations in boundary-fitted coordinate systems, J. Comput. Phys. 184 (2003) 299.
[35] T. Sarpkaya, Vorticity free surface and surfactants, Annu. Rev. Fluid Mech. 28 (1996) 83.
[36] R. Scardovelli, S. Zaleski, Direct numerical simulation of free-surface and interfacial flow, Annu. Rev. Fluid Mech. 31 (1999) 567.
[37] L.W. Schwartz, Computer extension and analytic continuation of Stokes' expansion for gravity waves, J. Fluid Mech. 62 (1974) 553.
[38] J. Sethian, P. Smereka, Level set methods for fluid interfaces, Annu. Rev. Fluid Mech. 35 (2003) 341.
[39] L. Shen, X. Zhang, D.K.P. Yue, G.S. Triantafyllou, The surface layer for free-surface turbulent flows, J. Fluid Mech. 386 (1999) 167.
[40] L. Shen, X. Zhang, D.K.P. Yue, G.S. Triantafyllou, Turbulent flow over a flexible wall undergoing a streamwise travelling wave motion, J. Fluid Mech. 484 (2003) 197.
[41] G.G. Stokes, On the theory of oscillatory waves, Trans. Camb. Philos. Soc. 8 (1847) 441.
[42] M.-Y. Su, Three-dimensional deep-water waves. Part 1. Experimental measurement of skew and symmetric wave patterns, J. Fluid Mech. 124 (1982) 73.
[43] P.P. Sullivan, J.C. McWilliams, C.-H. Moeng, Simulation of turbulent flow over idealized water waves, J. Fluid Mech. 404 (2000) 47.
[44] G. Tryggvason, B. Bunner, A. Esmaeeli, D. Juric, N. Al-Rawahi, W. Tauber, J. Han, S. Nas, Y.-J. Jan, A front-tracking method for computations of multiphase flow, J. Comput. Phys. 169 (2001) 708.
[45] W. Tsai, D.K.P. Yue, Computation of nonlinear free-surface flows, Annu. Rev. Fluid Mech. 28 (1996) 249.
[46] Y.-H. Tseng, J.H. Ferziger, A ghost-cell immersed boundary method for flow in complex geometry, J. Comput. Phys. 192 (2003) 593.
[47] Y.-H. Tseng, J.H. Ferziger, Large-eddy simulation of turbulent wavy boundary flow – illustration of vortex dynamics, J. Turbulence 5 (2004) 034.
[48] S.O. Unverdi, G. Tryggvason, A front-tracking method for viscous, incompressible, multi-fluid flows, J. Comput. Phys. 100 (1992) 25.
[49] D.T. Walker, R.I. Leighton, L.O. Garza-Rios, Shear-free turbulence near a flat free surface, J. Fluid Mech. 320 (1996) 19.
[50] M. Xue, Three-dimensional fully-nonlinear simulations of waves and wave body interactions, Ph.D. Thesis, Department of Ocean Engineering, Massachusetts Institute of Technology, 1997.

[51] M. Xue, H. Xü, Y. Liu, D.K.P. Yue, Computations of fully nonlinear three-dimensional wave–wave and wave–body interactions. Part 1. Dynamics of steep three-dimensional waves, J. Fluid Mech. 438 (2001) 11.
[52] J. Yang, E. Balaras, An embedded-boundary formulation for large-eddy simulation of turbulent flows interacting with moving boundaries, J. Comput. Phys. 215 (2006) 12.
[53] B. Yang, A. Prosperetti, A second-order boundary-fitted projection method for free-surface flow computations, J. Comput. Phys. 213 (2006) 574.
[54] D. Yang, L. Shen, Characteristics of coherent vortical structures in turbulent flows over progressive surface waves, Phys. Fluids 21 (2009) 125106.
[55] D. Yang, L. Shen, Direct-simulation-based study of turbulent flow over various waving boundaries, J. Fluid Mech. 650 (2010) 131.
[56] D. Yang, L. Shen, Simulation of viscous flows with undulatory boundaries: Part II. Coupling with other solvers for two-fluid computations, J. Comput. Phys. 230 (2011) 5510–5531.
[57] R.W. Yeung, Numerical methods in free-surface flows, Annu. Rev. Fluid Mech. 14 (1982) 395.
[58] R.W. Yeung, Nonlinear bow and stern wavesinviscid and viscous solutions, in: T. Miloh (Ed.), Mathematical Approaches in Hydrodynamics, SIAM Publisher, 1991, p. 349 (Chapter 24).
[59] R.W. Yeung, P. Ananthakrishnan, Viscosity and surface-tension effects on wave generation by a translating body, J. Eng. Math. 32 (1997) 257.
[60] H. Yuan, C.H. Wu, An implicit three-dimensional fully non-hydrostatic model for free-surface flows, Int. J. Numer. Methods Fluids 46 (2004) 709.
[61] Y. Zang, R.L. Street, J.R. Koseff, A non-staggered grid, fractional step method for time-dependent incompressible Navier–Stokes equations in curvilinear coordinates, J. Comput. Phys. 114 (1994) 18.
[62] C. Zhang, Turbulent free-surface wakes behind towed model – experimental measurements, numerical simulations and stability analysis, Ph.D. Thesis, Department of Ocean Engineering, Massachusetts Institute of Technology, 1996.
[63] C. Zhang, L. Shen, D.K.P. Yue, The mechanism of vortex connection at a free surface, J. Fluid Mech. 384 (1999) 207.
[64] D.P. Zilker, G.W. Cook, T.J. Hanratty, Influence of the amplitude of a solid wavy wall on a turbulent flow. Part 1. Non-separated flows, J. Fluid Mech. 82 (1977) 29.